Geophysical Journal International

Geophys. J. Int. (2020) **222,** 2084–2101
Advance Access publication 2020 June 11
GJI Seismology

doi: 10.1093/gji/ggaa284

Rayleigh-wave multicomponent crosscorrelation-based source strength distribution inversions. Part 2: a workflow for field seismic data

Zongbo Xu,[1] T. Dylan Mikesell,[1] Josefine Umlauft[2] and Gabriel Gribler[1]

[1] *Environmental Seismology Laboratory, Department of Geosciences, Boise State University, Boise, ID 83725, USA. E-mail: zongboxu@u.boisestate.edu*
[2] *Institute of Geophysics and Geology, Leipzig University, 04109 Leipzig, Germany*

Accepted 2020 June 8. Received 2020 April 20; in original form 2020 February 6

SUMMARY

Estimation of ambient seismic source distributions (e.g. location and strength) can aid studies of seismic source mechanisms and subsurface structure investigations. One can invert for the ambient seismic (noise) source distribution by applying full-waveform inversion (FWI) theory to seismic (noise) crosscorrelations. This estimation method is especially applicable for seismic recordings without obvious body-wave arrivals. Data pre-processing procedures are needed before the inversion, but some pre-processing procedures commonly used in ambient noise tomography can bias the ambient (noise) source distribution estimation and should not be used in FWI. Taking this into account, we propose a complete workflow from the raw seismic noise recording through pre-processing procedures to the inversion. We present the workflow with a field data example in Hartoušov, Czech Republic, where the seismic sources are CO_2 degassing areas at Earth's surface (i.e. a fumarole or mofette). We discuss factors in the processing and inversion that can bias the estimations, such as inaccurate velocity model, anelasticity and array sensitivity. The proposed workflow can work for multicomponent data across different scales of field data.

Key words: Waveform inversion; Seismic interferometry; Seismic noise; Surface waves and free oscillations.

1 INTRODUCTION

Knowledge of the ambient seismic source distribution (e.g. strength and location) is important in many research areas. For example, in investigating the subsurface with crosscorrelation-based seismic interferometry, one needs the source information to correct the empirical Green's functions or surface wave dispersion curves if the seismic sources are not isotropically distributed in all directions around sensors (e.g. Yao & van Der Hilst 2009; Nakata *et al.* 2015; Cheng *et al.* 2016). When monitoring changes in the subsurface with direct waves in seismic crosscorrelations, one needs to assess or revise the monitoring results based on changes in the seismic source(s) (e.g. Delaney *et al.* 2017; Takano *et al.* 2019). In addition, spatial and temporal distributions of natural seismic sources (e.g. ocean microseism) can aid studies of the actual source mechanism (e.g. Cessaro 1994; Juretzek & Hadziioannou 2016).

To investigate the ambient (noise) seismic source distribution, one can use a traditional imaging method or an adjoint-based inversion method. The imaging methods (e.g. matched-field processing) mainly focus on the source location, and do not provide physical source properties like strength or amplitude (e.g. Cros *et al.* 2011). In contrast, the adjoint-based inversion method can estimate both source location and strength. Tromp *et al.* (2010) and Fichtner *et al.* (2017) derived an adjoint for crosscorrelations, and Ermert *et al.* (2017) applied this crosscorrelation adjoint to long period (over 100 s) seismic crosscorrelations to study Earth's hum. For seismic sources such as tremors and ambient seismic sources, there are usually no clear body-wave arrivals in the seismic recordings and mainly traditional imaging methods have been applied to the seismic crosscorrelations (e.g. Obara 2002; Zeng & Ni 2010; Corciulo *et al.* 2012), largely composed of surface waves.

To make a comparison between traditional methods and the adjoint-based inversion, Xu *et al.* (2019) show that the matched-field processing method can be written as the crosscorrelation waveform-adjoint sensitivity kernel with zero initial sources. For surface wave studies, Xu *et al.* (2019) further demonstrated that Rayleigh-wave multicomponent crosscorrelations can better constrain estimation of the source distribution compared to vertical-component crosscorrelations alone. The multicomponent data are vertical (*Z*) and radial (*R*) components, where the *R* direction is parallel to a line or great-circle path between two sensors. We refer to the crosscorrelation adjoint inversion for seismic sources as the *source inversion method* in this paper.

The source inversion method is well developed in theory, but in practice still requires pre-processing of the raw seismic recordings. Some procedures are the same as the pre-processing in ambient noise tomography (ANT, Shapiro *et al.* 2005), such as stacking and excluding high-amplitude transient signals (i.e. earthquakes). However, there are some differences between the two sets of pre-processing procedures because the final goal of ANT is to image structure (i.e. velocity models), which is different from the source inversion method used to image source distributions. For example, if one inverts for Earth's hum, one has to remove not only earthquakes, but also the primary microseism, which is normally the signal source for ANT. In addition, the seismic source inversion method requires known Green's functions, while the focus of ANT is to recover Green's functions. It is easy to misuse some ANT pre-processing procedures (e.g. normalization) in seismic source studies (e.g. Tian & Ritzwoller 2015) and these procedures can bias the consequent source estimation (e.g. Fichtner *et al.* 2017). Thus the purpose of this study is to present clear data pre-processing procedures in a workflow for the source inversion method. We use an L_2 waveform misfit function in the inversion, and we use observed ambient seismic noise data in the Hartoušov mofette field (Fig. 1), Czech Republic, as a field data example to demonstrate the workflow. The parameters in the workflow are easy to adjust based on different field scales.

We introduce the workflow from raw seismic recordings to the source inversion. In the crosscorrelation adjoint-based inversion used here (e.g. Ermert *et al.* 2017; Xu *et al.* 2019), there are two major assumptions:

1.the subsurface structure is known (i.e. the Green's function is known);
2.all potential seismic sources share a similar shape in terms of energy spectral density.

Thus in the workflow, we need to estimate both Green's function for the subsurface media and the source energy spectral density shape (Section 2). We then estimate the spatial source distribution of fumaroles from the field data, and compare our estimation to a field CO_2 flux map (Section 3). We finally discuss the effect of inaccurate subsurface models, especially the anelastic property, and insufficient sensitivity of the data to the source estimation (Section 4).

2 WORKFLOW

We introduce the workflow in four steps (Fig. 2). We first select data (i.e. observed crosscorrelations) based on a signal-to-noise ratio (SNR) criteria; then we process the data to isolate targeted source types (Section 2.1). We estimate Green's functions (Section 2.2) and present a novel method to calculate source energy spectral density shape (Section 2.3). After these three steps, we introduce the source waveform inversion briefly (Section 2.4). The whole workflow is applicable for not only vertical component (Z), but also radial (R) component seismic recordings. Thus we can use Z–Z component crosscorrelations (C_{ZZ}) and/or R–R component crosscorrelations (C_{RR}) in the workflow.

2.1 Data selection and crosscorrelation

We refer to the crosscorrelations as the *data* in this source inversion method. Counter to normal ambient seismic crosscorrelations for ANT, as our focus is the ambient source location(s) and strength(s), thus we do not apply time-domain or frequency-domain normalization to the raw data prior to crosscorrelation because these procedures bias the source estimation result (e.g. Fichtner *et al.* 2017). Without the common ANT processing procedures, however, the crosscorrelations for a seismic source study will be far from the true Green's functions if the source distribution is anisotropic. In this case, direct body and surface waves can arrive any time between time zero and the true (i.e. physical) direct-wave arrival time (e.g. Shapiro *et al.* 2006; Snieder & Fleury 2010). The events that arrive before the true direct wave are called spurious or non-physical arrivals under the assumption that the crosscorrelation approximates the Green's function (e.g. Mikesell *et al.* 2009; Snieder & Fleury 2010). In contrast to ANT though, the spurious energy here is actually the important signal, used in the inversion to estimate the seismic source distribution.

In addition to so-called spurious arrivals in the crosscorrelations, noise can also be strong and thus affect the source estimation. This noise can consist of (1) uncorrelated random noise and (2) untargeted seismic-source waves, which can be in a similar frequency band as the targeted seismic sources. For the uncorrelated random noise, one can use stacking to suppress this noise, similar to the ANT processing (e.g. Bensen *et al.* 2007). We use linear stacking here, which is common and does not distort information contained in the crosscorrelation waveforms. Some stacking methods, such as phase-weighted stacking (Schimmel & Paulssen 1997), do distort the waveforms and thus affect the inversion results. Besides linear stacking, we could also select high-SNR crosscorrelations from the targeted sources in stacking (e.g. Cheng *et al.* 2016), but we do not do that here. Instead we use a single consistent amount of time, over which the targeted source dominates the crosscorrelations. Choosing this time window is based on analysis of the SNR of the linear crosscorrelation stack as we add more time.

One could use a SNR criterion to choose the crosscorrelations with the least uncorrelated noise among all crosscorrelations (e.g. Lin *et al.* 2008). However, we propose here a SNR measurement similar to the SNR measurement algorithm in ANT (e.g. Bensen *et al.* 2007). We set two time windows—a signal and a noise window. As stated above, the direct wave signal can arrive between time zero and the true arrival time, thus our signal window is different from the signal window in the ANT SNR algorithm, where the signal window is around the true surface wave arrival time. We set our signal window be a wide time window that ranges from the acausal to causal times, encompassing our estimate of the slowest possible physical surface wave arrivals (–2 to 2 s in Fig. 3 for the fumarole example). For our noise window, we select two noise windows outside the signal window on both causal and acausal branches of crosscorrelations (–5 to –3 s and 3–5 s in Fig. 3). The noise windows are away from the signal time window by one second in our case. We calculate the SNR as the ratio between the peak value in the signal window and the RMS value in the two noise windows. We set an SNR>15 criterion to select the crosscorrelations which we use in the source inversion method. The time parameters, such as time window length, in the SNR measurements need to be adjusted based on different field data and array properties (e.g. interstation spacing).

It is also necessary to separate the untargeted seismic-source waves from the signal of interest as much as possible. Stacking works to suppress uncorrelated random noise, but can increase the amplitude of untargeted seismic-source waves (e.g. Shapiro *et al.* 2006; Zeng & Ni 2010). Thus the source inversion will not only image the targeted seismic source, but also any untargeted seismic sources. Therefore it is important to reduce or remove the untargeted

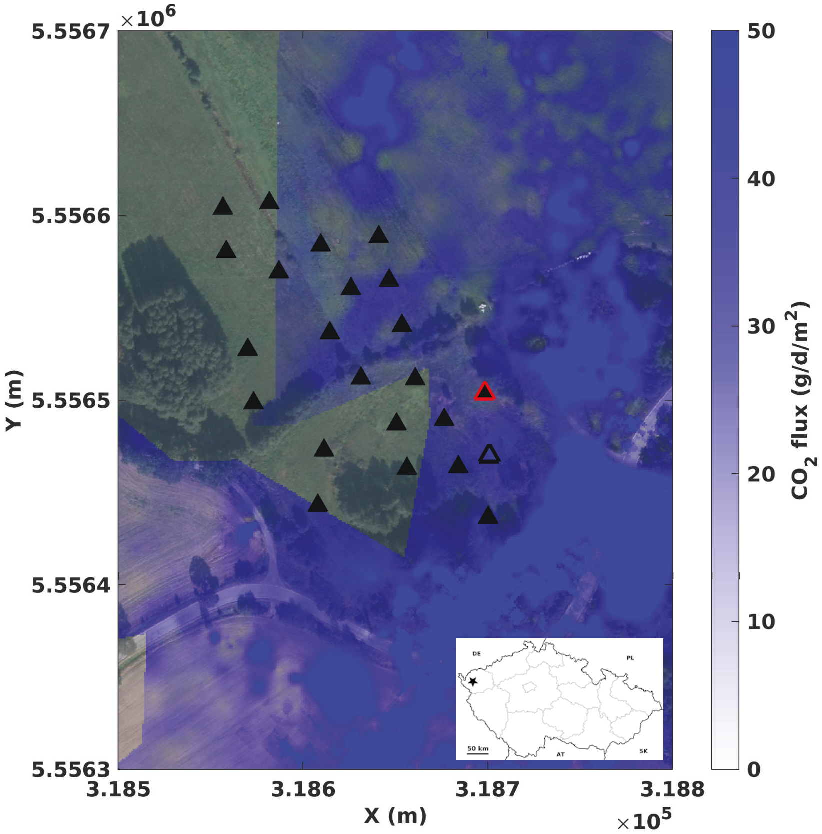

Figure 1. A site map of the seismic array and CO_2 gas-flux distributions. Each triangle is a geophone. The empty triangle is the noisy one. The red-edge triangle is the C601 sensor in Fig. 4. The gas-flux data are from Nickschick *et al.* (2015) and were acquired from 2007 to 2013. The star in the inset shows the site location in the Czech Repulic. The coordinates are in WGS84/UTM zone 33.

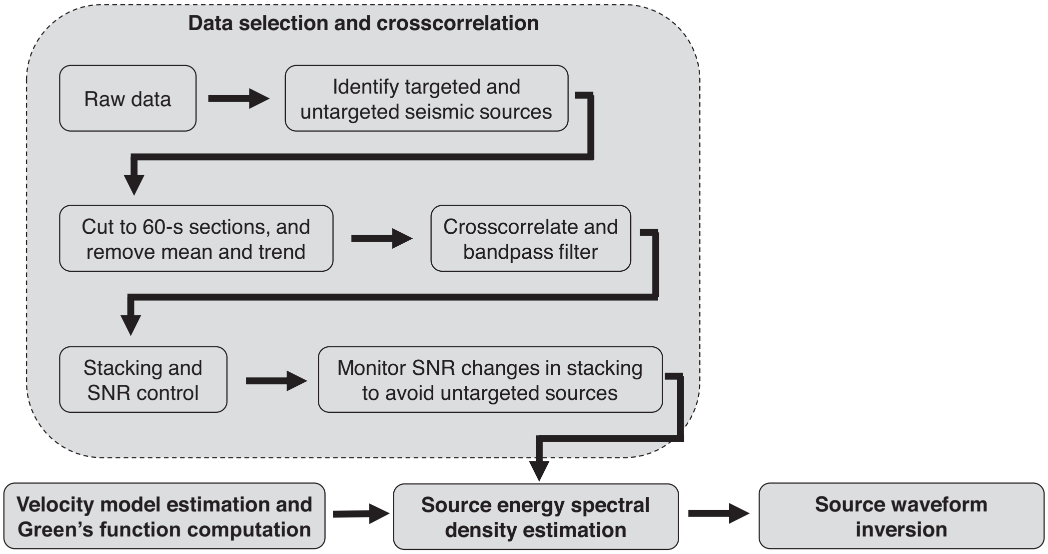

Figure 2. The source inversion workflow is divided into four steps: data selection and crosscorrelation (Section 2.1), velocity model estimation and Green's function computation (Section 2.2), source energy spectral density estimation (Section 2.3) and the source waveform inversion (Section 2.4).

seismic-source waves. For continental-scale source studies like for microseisms, earthquake events are usually the strongest among all correlated sources and need to be removed (e.g. Ermert *et al.* 2017). At the near-surface scale, as in this fumarole example, the untargeted seismic-source waves are mainly due to anthropogenic activity (e.g. traffic) and ground-coupled tree vibrations. Unfortunately, these untargeted seismic sources and the fumaroles can both emit high-frequency (>2 Hz) Rayleigh and/or body wave energy (Cheng *et al.* 2016; Estrella *et al.* 2016; Roux *et al.* 2018). We avoid the tree vibrations by using data above the tree resonance fre-

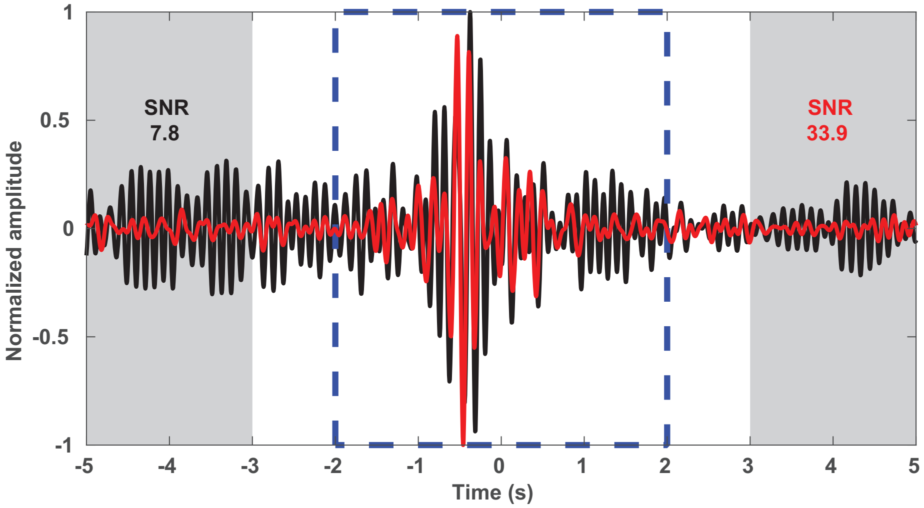

Figure 3. An example of the SNR measurement. The blue dashed box indicates the signal window. The two grey areas indicate the two noise windows. SNR is defined as the ratio of the peak in the signal window and the RMS in the two noise windows. We combine the recordings in the two noise windows and then calculate the RMS from the combined recordings. The black (left-hand side) and red (right-hand side) numbers in the grey areas indicate the SNR for the two waveforms, respectively. The waveforms are bandpass filtered between 3.5 and 10 Hz.

quency, approximately 2 Hz (e.g. Roux *et al.* 2018), and we avoid the anthropogenic activity by using data recorded during the night when there is less anthropogenic activity compared to daytime (e.g. Yamanaka *et al.* 1993).

We first analyse the ambient seismic recordings from 01:00 to 04:00 local time on 23 November 2016. During this time period, there are usually smaller wind speeds in inland areas than daytime (e.g. He *et al.* 2013) which also reduces the likelihood of tree vibrations, and we assume that the main seismic sources during this time are fumaroles. We divide the 3-hr long raw data (01:00–04:00) into 60-s sections; then we remove the mean and linear trend in each section. Because all of the sensors in the array are the same, we do not need to remove the instrument response. We crosscorrelate these sections and bandpass filter the crosscorrelations between 3.5 and 10 Hz. We then stack crosscorrelations for each sensor pair. We monitor the SNR improvement as we stack more sections and find that the SNR drops dramatically around 03:30 (Fig. 4a) in both C_{ZZ} and C_{RR}. The drop indicates that the number of station pairs with high-SNR (>15) crosscorrelations decreases. This SNR change is due to a different strong seismic source (Figs 4b and c), which has changed the crosscorrelation dramatically. This transient source could be human activity or another fumarole. If one looks more closely at the number of stations pairs, there are a few other small drops that are related to other high-amplitude transient signals. We do not investigate these transient signals further, but because of this large drop in SNR, we do not use the raw data after the 03:30 and study only the ambient seismic recordings from 01:00 to 03:30, a total of 2.5 hr, in this source inversion example. Note that the SNR increases without the drop if we skip the recordings between 03:30 and 03:35, and drop again afterwards around 4:20 (Fig. S1). This observation indicates that we could conduct a more sophisticated stacking than the linear stacking, but this topic is beyond the research scope in this paper.

We also winnow the C_{ZZ} waveforms based on the interstation distance. Small interstation-distance C_{ZZ} waveforms are less sensitive to source changes compared to large-distance waveforms (Appendix A). Furthermore, the *ZZ* sensitivity kernels do not change much with source changes when the interstation distance is small. However, due to the azimuth effect of the *R* component (e.g. Haney *et al.* 2012; Xu & Mikesell 2017; Xu *et al.* 2019), the small-distance C_{RR} waveforms are still sensitive to source changes and help constrain source locations (Appendix A). Thus the small-distance C_{ZZ} waveforms do not add much benefit to the source inversion, but C_{RR} waveforms do. Therefore we ignore small-distance C_{ZZ} waveforms, but do not ignore C_{RR} waveforms with small interstation distances. In this study, we use C_{ZZ} waveforms when the interstation distance is larger than 50 m, which is about the longest Rayleigh-wave wavelength in our study.

2.2 Velocity model estimation and Green's function computation

Seismic source studies commonly assume that the subsurface velocity model is known and thus use Green's functions based on the assumed velocity model. For the continental-scale source studies, one can choose a reference velocity model, like AK135 (Kennett *et al.* 1995). However, for near-surface studies, one usually does not have a reference model and thus has to estimate the velocity model somehow. There are many approaches to estimate near-surface velocity models from ambient seismic data (e.g. Lin *et al.* 2013; Cheng *et al.* 2015). In this example, we estimate Rayleigh-wave phase velocities (Appendix B) and then use the phase velocities to calculate Green's functions. We assume that the subsurface at the Hartoušov field is laterally homogeneous, isotropic and elastic and thus use the far-field Rayleigh-wave Green's function from a vertical-force source to generate synthetic waveforms in the inversion:

$$G_{ZZ}(r,\omega) = \sqrt{\frac{1}{8\pi\omega r/c(\omega)}}\mathrm{e}^{-i(\omega r/c(\omega)+\pi/4)}, \quad (1)$$

and

$$G_{RZ}(r,\omega) = \frac{H(\omega)}{V(\omega)}\sqrt{\frac{1}{8\pi\omega r/c(\omega)}}\mathrm{e}^{-i(\omega r/c(\omega)-\pi/4)}, \quad (2)$$

where i is the imaginary unit, $c(\omega)$ is the surface wave phase velocity, and r is the distance between the source and receiver. $H(\omega)/V(\omega)$ is the ratio of the horizontal-to-vertical motion (e.g.

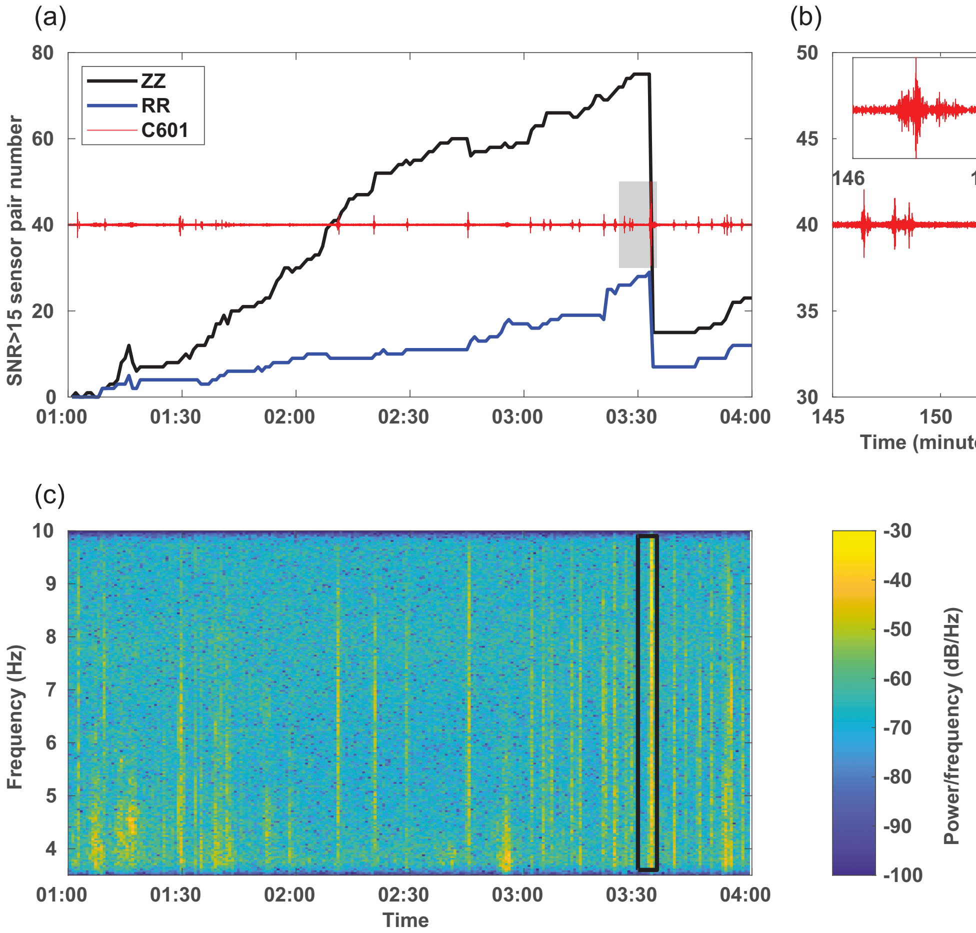

Figure 4. (a) The number of sensor pairs with SNR > 15 changes with time as we stack more time sections of crosscorrelations. The time axis is from 01:00 to 04:00 on 23 November 2016. The red line is the continuous seismic recording for the C601 geophone during this time period. The recording is bandpass filtered between 3.5 and 10 Hz. (b) A zoom of the continuous recording in the grey area in (a). The inset shows a zoom of the first event. (c) The spectrogram of the C601 continuous recording in (a) from the short-time Fourier transform; the window for the Fourier transform is 60 s. The high-power signal in the black box corresponds to the strong transient signal in (b) and causes the drop in the ZZ and RR curves in (a).

Haney *et al.* 2012). These two Green's functions use the Rayleigh-wave phase velocity function from Appendix B and the $H(\omega)/V(\omega)$ from Section 2.3. Note that although accurate Green's functions are important for seismic source studies, our focus for this paper is the whole workflow for the source inversion, instead of estimating accurate individual Green's functions. We discuss the notion estimating both sources and structure together in Section 4.1. In addition, for laterally heterogeneous media, one can use wave equation solvers to compute Green's functions rather than use the analytic models presented here (e.g. Ermert *et al.* 2017; Sager *et al.* 2018).

2.3 Source energy spectral density estimation

We assume that all seismic sources share a similar energy spectral density shape (S_p^0). This assumption is valid in that the same types of natural ambient seismic sources possess a similar source mechanism, such as a river (e.g. Tsai *et al.* 2012) or an ocean (e.g. Ardhuin *et al.* 2011). This assumption decreases the potential model space because we only need a ratio (N) to indicate the strength of each potential source (e.g. Ermert *et al.* 2017; Xu *et al.* 2019). To estimate S_p^0, we present a novel, data-driven approach.

We write the autocorrelation for each sensor as

$$C_{mm}(r_A,\omega) = \int_V G_{mp}(r_A,r_s,\omega)G^*_{mp}(r_A,r_s,\omega)S_p(\omega)\mathrm{d}r_s,$$
$$= S_p^0(\omega)\int_V |G_{mp}(r_A,r_s,\omega)|^2 N(r_s)\mathrm{d}r_s, \tag{3}$$

where S_p and S_p^0 are non-negative (e.g. Xu *et al.* 2019). We then combine the autocorrelation (eq. 3) and the far-field Rayleigh-wave Green's functions (eqs 1 and 2) as

$$C_{ZZ}(r_A,\omega) = S_Z^0(\omega)\int_V \frac{1}{8\pi\omega r_{As}/c(\omega)}N(r_s)\mathrm{d}r_s$$
$$= \frac{S_Z^0(\omega)}{\omega/c(\omega)}\int_V \frac{N(r_s)}{8\pi r_{As}}\mathrm{d}r_s, \tag{4}$$

and

$$C_{RR}(r_A,\omega) = S_Z^0(\omega)\int_V \left[\frac{H(\omega)}{V(\omega)}\right]^2 \frac{1}{8\pi\omega r_{As}/c(\omega)}N(r_s)\mathrm{d}r_s$$
$$= \frac{S_R^0(\omega)}{\omega/c(\omega)}\int_V \frac{N(r_s)}{8\pi r_{As}}\mathrm{d}r_s, \tag{5}$$

where r_{As} is the distance between a source (r_s) and the receiver (r_A). Noting that $S_R^0(\omega) = [H(\omega)/V(\omega)]^2\, S_Z^0(\omega)$. The integral over V in eqs (4) and (5) represents a geometric relationship between the receiver and all seismic sources. The integral is independent of frequency, and thus we can write this integral as an amplitude normalization constant

$$D(r_A) = \int_V \frac{N(r_s)}{8\pi r_{As}} \mathrm{d}r_s. \tag{6}$$

Finally, we write:

$$S^0_Z(\omega) = \frac{\omega C_{ZZ}(r_A, \omega)}{c(\omega) D(r_A)}, \tag{7}$$

$$S^0_R(\omega) = \frac{\omega C_{RR}(r_A, \omega)}{c(\omega) D(r_A)}. \tag{8}$$

We estimate $S^0_Z(\omega)$ and $S^0_R(\omega)$ using the same raw ambient seismic data in the observed crosscorrelations. We calculate the autocorrelations (C_{ZZ}, $C_{RR} = C_{EE} + C_{NN}$) for each sensor following the processing procedures in Section 2.1. We then transform the autocorrelations to the frequency domain. For each *ZZ* autocorrelation we normalize by the value of that autocorrelation at the lowest targeted frequency (*D* in eqs 7 and 8). For the corresponding *RR* autocorrelation we normalize by the *ZZ* value to preserve the H/V information. We then average the normalized autocorrelations among different sensors. We multiply the averaged autocorrelation with $\omega/c(\omega)$ to estimate $S^0_Z(\omega)$ and $S^0_R(\omega)$ (Fig. 5). The S^0_Z is different from S^0_R due to the $H(\omega)/V(\omega)$ ratio as noted previously. Note this estimation approach is for laterally homogeneous, isotropic and elastic media. For heterogeneous media, one can choose a Gaussian spectrum to approximate S^0_Z in a narrow frequency band (e.g. Ermert *et al.* 2017; Sager *et al.* 2020).

2.4 Source waveform inversion scheme

We are now ready to conduct the source inversion after the three previous steps. The inversion scheme has already been stated in detail (e.g. Ermert *et al.* 2017; Xu *et al.* 2019). Thus we describe the whole scheme briefly here. Note one can define the misfit function not only on crosscorrelation waveforms as we do, but also on crosscorrelation symmetry (e.g. Ermert *et al.* 2015) or on crosscorrelation envelope (e.g. Fichtner *et al.* 2008; Bozdağ *et al.* 2011). We choose the waveform misfit function because the waveform inversion can potentially recognize multiple seismic sources (e.g. Xu *et al.* 2019). We define an L_2-norm waveform misfit function and present both the time- and frequency-domain versions, respectively:

$$\chi = \frac{1}{2} \sum_{mn} \sum_{r_A r_B} \int [w(t)(C_{mn}(r_A, r_B, t) - C^o_{mn}(r_A, r_B, t))]^2 \mathrm{d}t, \tag{9}$$

$$= \frac{1}{2} \sum_{mn} \sum_{r_A r_B} \int |w(\omega) *_\omega (C_{mn}(r_A, r_B, \omega) - C^o_{mn}(r_A, r_B, \omega))|^2 \mathrm{d}\omega, \tag{10}$$

where $w(t)$ is a time window, $*_\omega$ denotes a convolution in the frequency domain and $C_{mn}(r_A, r_B, t)$ and C^o_{mn} are the synthetic and observed crosscorrelations, respectively. The crosscorrelations are between sensor r_A and r_B; m, n represent the components, vertical (Z) or radial (R), from each of the two sensors, respectively. One can also use the transverse component here if the noise source is thought to generate Love waves. We apply a global normalization to each set of crosscorrelations. For example, we normalize all C_{ZZ} by the global maximum value of C_{ZZ} from all available sensors pairs. We normalize C_{RR} in the same manner, taking the global maximum value of C_{RR} from all available sensor pairs.

We use the time window in eq. (10) to focus on the main arrivals in the observed crosscorrelations (e.g. Maggi *et al.* 2009; Fichtner *et al.* 2017). We set the time window to be the signal window in our SNR measurement (Section 2.1). We calculate the observed crosscorrelations as described in Section 2.1. We calculate the synthetic crosscorrelations in the frequency domain as

$$C_{mn}(r_A, r_B, \omega) = \int_V G_{mp}(r_A, r_s, \omega) G^*_{np}(r_B, r_s, \omega) S^0_p(\omega) N(r_s) \mathrm{d}r_s \tag{11}$$

where $G_{mp}(r_A, r_s, \omega)$ is the Green's function representing the mth component displacement response at location r_A due to a point force in the p direction at the source position r_s, ω is the angular frequency, and the asterisk denotes complex conjugation. We estimate the Green's functions in Section 2.2 and $S^0_p(\omega)$ in Section 2.3. In this study, we create a potential source grid that is 41 by 41 elements with a 5 m grid distance. We also assume that all sources only emit vertical-direction forces on Earth's surface.

In order to minimize the misfit function and ensure non-negative solutions, we apply an iterative waveform inversion methodology to update the ambient noise source distribution model (N). We minimize the waveform misfit function using a gradient-descent strategy (e.g. Ermert *et al.* 2017; Xu *et al.* 2019). The gradient is a sum of source sensitivity kernels over the chosen sensor pairs

$$K(r_s) = \sum_{mn} \sum_{r_A r_B} \int_{\omega_1}^{\omega_2} K_{mn}(r_A, r_B, r_s, \omega) \mathrm{d}\omega. \tag{12}$$

If we only use vertical data, K is a summed K_{ZZ}; if we use both C_{ZZ} and C_{RR}, $K = K_{ZZ} + K_{RR}$ among the chosen sensor pairs. We normalize K by the maximum of absolute values in K. We write the waveform source kernel for a sensor pair as

$$K_{mn}(r_A, r_B, r_s, \omega) = G_{mp}(r_A, r_s, \omega) G^*_{np}(r_B, r_s, \omega) S^0_p f, \tag{13}$$

where f is the adjoint source (e.g. Fichtner 2015; Ermert *et al.* 2017; Xu *et al.* 2019). The adjoint source is derived from the waveform misfit function as

$$f(\omega) = \frac{1}{\pi}[w(\omega) *_\omega w(\omega) *_\omega (C_{mn}(r_A, r_B, \omega) - C^o_{mn}(r_A, r_B, \omega))]^*, \tag{14}$$

where $w(\omega)$ is the window function. We update the source strength distribution as

$$N_{i+1}(r_s) = N_i(r_s) \mathrm{e}^{-\beta N_i(r_s) K(r_s)}, \tag{15}$$

which is written this way to ensure positivity (e.g. Johansen 1977; Xu *et al.* 2019). We choose the step size (β) from many potential step size values (e.g. $\beta = 10^{-3}$, 10^{-2}, ...10^2). For each step size we generate an updated source distribution model (N_{i+1}). We apply a 2-D Gaussian smoothing filter to the updated model, where the standard deviation of the filter is the length of one source grid, 5 m, and compute synthetic crosscorrelations using eq. (11). We then calculate the corresponding misfit. Among these misfit values, we choose the step size that gives the minimum misfit; this is the common *line-search method*. If the new minimum misfit is less than 99 per cent of the misfit in the last step, we adopt the step size and update the source model; if not, we do not update this iteration and instead expand the frequency band. We start from 4.5–6 Hz and then extend to 4.5–9 Hz.

3 FIELD DATA EXAMPLE

We process the ambient seismic recordings in the Hartoušov mofette field, Czech Republic, as a near-surface example. Mofettes or

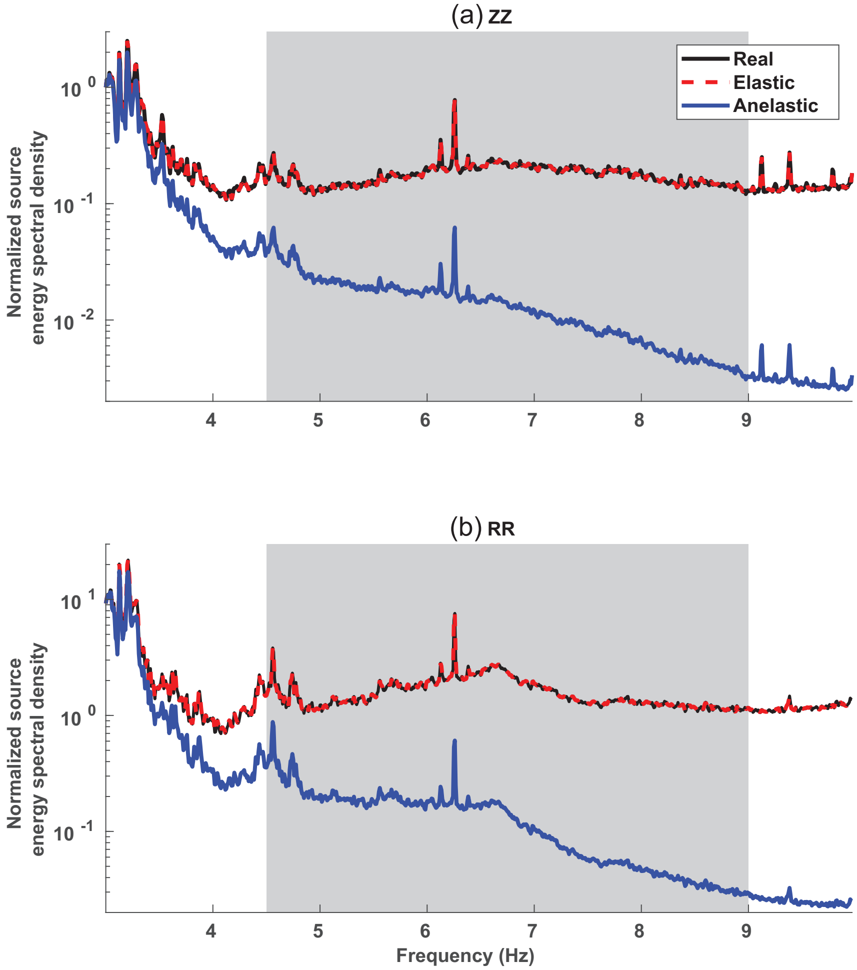

Figure 5. Normalized source energy spectral density estimations, S_Z^0 and S_R^0. We estimate S_Z^0 (a) and S_R^0 (b) (black lines) from the field data waveform autocorrelations C_{ZZ} and C_{RR}, respectively. We then use the two estimates in the forward model. In the forward model, if we use the elastic Green's functions (eqs 1 and 2), our estimated source energy spectral densities (red dashed lines) are the same shape as the real source energy spectral density. If we use the anelastic Green's functions, we estimate incorrect densities (blue lines). Here the spectral density is for displacement wavefield (Appendix C). The grey areas indicate the frequency range we use in the waveform inversion, 4.5–9 Hz. Note here that we only focus on the shape, instead of the absolute values among real, elastic and anelastic estimations. All S_Z^0 and S_R^0 in this figure are normalized by the S_Z^0 at the lowest frequency.

fumaroles, are openings in Earth's surface where carbon dioxide (CO_2) flows from depths to the free surface and then escapes. This CO_2 degassing phenomenon generates high-frequency seismic waves at depth and at the free surface (e.g. Estrella *et al.* 2016; Bussert *et al.* 2017). The seismic waves behave like tremor (e.g. Umlauft & Korn 2019) and thus in order to estimate the mofette distributions, we can use the source waveform inversion. We test the inversion with both synthetic and field data.

A seismic observation was conducted at the Hartoušov mofette field, Czech Republic (Umlauft & Korn 2019). The seismic observations are continuous from 21 to 24 November 2016. In this paper we use a subset of the observation, a subarray that consists of 23 three-component 4.5-Hz geophones (Fig. 1). The recording sample rate is 250 Hz and we downsample the data to 200 Hz to speed the crosscorrelation process. We abandon one of the 23 geophones because there is too much noise at the station. Thus we use the 22 geophones to estimate the ambient seismic source distribution. The area under the array is relatively flat. The maximum elevation difference is 1.5 m, which is negligible compared to the shortest wavelength we use in this study, about 20 m. Through the data selection (Section 2.1), we end up with 47 C_{ZZ} and 22 C_{RR} as the observed crosscorrelations, noting that we only use *RR* data that also had *ZZ* data to ensure we focus on the Rayleigh wave.

3.1 Synthetic data tests

We examine our estimation algorithm for S_p^0 and the subsequent inversion for $N(r_s)$ with synthetic data first to understand the resolution limits of the 22-station array. We also compare the synthetic waveform inversions with and without the smoothing filter because in practice one commonly smooths the model in the waveform inversion for structures (e.g. Tape *et al.* 2007; Groos *et al.* 2017), and here we investigate the effectiveness of smoothing in the waveform inversion for sources. We use the same array and same available sensor pairs as in the field data (47 C_{ZZ} and 22 C_{RR}). We create a source strength distribution model with two in-array seismic sources (e.g. Fig. 6a). We use synthetic data generated with an elastic model as the observed data and thus use elastic Rayleigh-wave Green's functions (eqs 1 and 2) in the inversion. We use the Rayleigh-wave phase velocities from the field data (Fig. B1) in the Green's functions; then use the source energy spectral den-

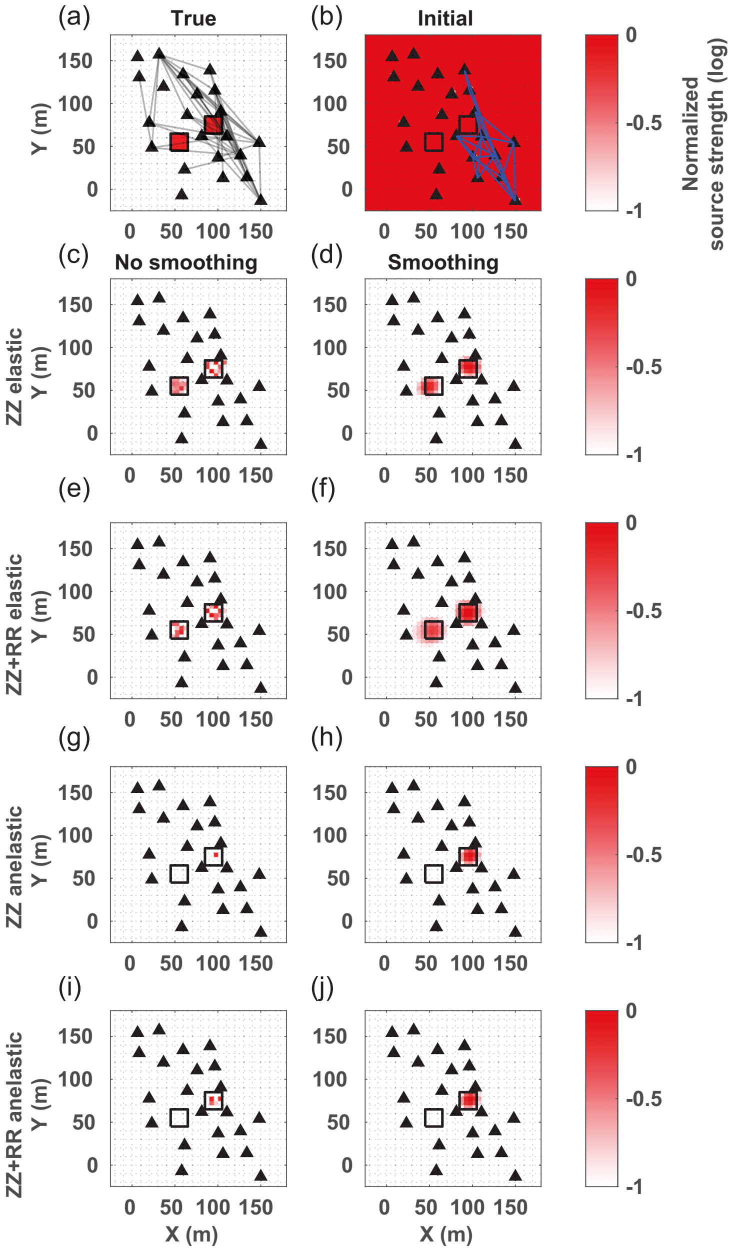

Figure 6. The elastic and anelastic synthetic data inversion results. (a) The true source strength is zero everywhere except for the two source areas within the array. Each triangle represents a geophone. From an initial source model (b), for the elastic synthetic crosscorrelations, we invert *ZZ* waveforms with and without smoothing (c and d, respectively) and *ZZ* + *RR* waveforms with and without smoothing (e and f, respectively). For the anelastic synthetic crosscorrelations, we invert *ZZ* waveforms with and without smoothing (g and h, respectively) and *ZZ* + *RR* waveforms with and without smoothing (i and j, respectively). The empty squares indicate the true source areas. The grey lines in (a) indicate the 47 available C_{ZZ} sensor pairs; the blue lines in (b) indicate the 22 available C_{RR} sensor pairs that passed the data selection criteria.

sity shapes (S_Z^0 and S_R^0) from the raw data (black lines in Fig. 5) to calculate synthetic crosscorrelations (eq. 11) and autocorrelations (eq. 3). Prior to the inversion, we apply our algorithm to estimate the source energy spectral densities (Section 2.3). We observe that we recover the correct source energy spectral densities (red dashed lines in Fig. 5). This observation fits our theory. Note the peaks in the spectra (Fig. 5) do not affect the source inversion because the inversion already incorporates the spectra as S_Z^0 and S_R^0 in eq. (13).

After estimating the source energy spectral densities, we use the elastic synthetic data as the observed data and do the waveform inversion (Fig. 6). For the elastic data, we obviously use the correct S_Z^0 and S_R^0 (red dashed line in Fig. 5) in the waveform inversions. We observe that the *ZZ* + *RR* inversion result (Fig. 6e) is closer to the true source model than the *ZZ* inversion result (Fig. 6c) if we do not use the smoothing filter. However, with smoothing, the *ZZ* + *RR* gives a similar inversion result (Figs 6 d and f) and a similar final misfit to *ZZ* (Table 1). Hence smoothing acts to sup-

Table 1. Final waveform inversion misfits from the *ZZ*/*ZZ* + *RR* inversions in the synthetic data tests. We show the final misfits in the 4.5–9 Hz band relative to the initial misfit (eq. 10). The number of iterations is provided in parenthesis next to the mistfit value. The two-source elastic examples are presented in Section 3.1 and the other examples are presented in Section 4.

Method	Elastic without smoothing	Elastic with smoothing	Anelastic without smoothing	Anelastic with smoothing
Two-source example	0.08(21)/0.10(15)	0.09(2)/0.10(4)	0.52(2)/0.43(3)	0.27(2)/0.34(2)
Out-of-array source	–	–	–	0.41 (2)/0.24(3)
Three-source example 1	–	0.13(4)/0.12(3)	–	–
Three-source example 2	–	0.24(3)/0.20(7)	–	–
Three-source example 3	–	0.08(14)/0.10(7)	–	–

Table 2. Final waveform misfits from *ZZ* and *ZZ* + *RR* waveform inversions on the Hartoušov crosscorrelations. We show the the final misfit in the 4.5–9 Hz band. Misfit values are relative to the initial misfit (eq. 10) in each case.

Data	Iteration	C_{ZZ}	C_{RR}	C_{ZZ} and C_{RR}
ZZ inversion	5	0.63	0.58	0.61
ZZ + *RR* inversion	4	0.69	0.47	0.62

press the improved resolution from the *RR* sensitivity kernels while helping to recover the shape of seismic sources within fewer iterations (Table 1). Therefore, we adopt the smoothing in the waveform inversion of the field data, recognizing that our results are perhaps overly smeared.

3.2 Source inversion results

We apply the waveform inversion to the Hartoušov observed data – 47 C_{ZZ} and 22 C_{RR} waveforms, after the pre-processing procedures (Sections 2.1–2.3). We use the estimated source energy spectral densities (black lines in Fig. 5) in the forward model. We compare the different waveform misfits for the different inversion models in Table 2. For example, the waveforms from the *ZZ* inversion (Fig. 7a) fit the observed C_{ZZ} well, but do not fit the observed C_{RR} as well as the *ZZ* + *RR* inversion (Table 2 and Fig. 8). The *ZZ* + *RR* inversion model gives a similar misfit for C_{ZZ} waveforms and also a similar total misfit for C_{ZZ} and C_{RR} compared to the *ZZ* inversion. The *ZZ* inversion result (Fig. 7b) indicates one strong and two weak (east and west) sources. However, the *ZZ* + *RR* inversion only indicates one source in a similar location as the west weak source in the *ZZ* model (Fig. 9b). Note that the *ZZ* + *RR* inversion result explains both C_{ZZ} and C_{RR} waveforms, while the *ZZ* model only explains the C_{ZZ} waveforms. Thus the one source estimation from the *ZZ* + *RR* inversion is more reasonable than the *ZZ* inversion result. Moreover, based on a synthetic test in Section 4.1, the strong source in the *ZZ* result is likely due to the anelasticity of the subsurface. We further confirm the ZZ+RR inversion result by conducting the inversions on a different initial model; this helps discern the role of the starting model and can help identify if the inversion is in a local minimum related to the starting model. Using the new starting model, we achieve a similar result to the ZZ+RR inversion result (Fig. S2). As another check, we find that the source location in the ZZ+RR inversion result explains some of the transient event moveouts across the array. This indicates that the transient events could very well originate from the inverted source location (Fig. S4).

Besides the seismic data analysis, we use the CO_2 flux data to validate our inversion results. On top of the inversion results, we overlay the CO_2 flux map (Nickschick *et al.* 2015) collected 3 yr before the seismic data here. The strong source in the *ZZ* result is not close to any strong CO_2 gas areas, acknowledging that we lack complete data coverage of the gas data. However, the common source in the *ZZ* and *ZZ* + *RR* results is near the strong gas sources to the East (i.e. fluxes >50 g d^{-1} m^{-2}), but does not perfectly coincide with a high gas-flux area measured 3 yr prior. The location bias for the common source could be due to our simplified 1-D velocity model and/or the source actually occurring at depth or moving laterally since the gas data were collected. We revisit the potential velocity model bias in Section 4.1, but we assume that all seismic sources are on the Earth's surface in this workflow, even though the CO_2 flux can generate seismic energy at depth (e.g. Bussert *et al.* 2017; Umlauft & Korn 2019). Both of these potentially invalid assumptions can lead to location biases. However we also note that the CO_2 data were not acquired at the same time as the seismic data, and mofettes/fumaroles are known to turn on and off through time (e.g. Nickschick *et al.* 2015).

Based on the waveform misfits and the location of strong degassing, our conclusion is that the common source in the *ZZ* and *ZZ* + *RR* inversion results is likely a seismic source (or small region of sources) active during the 2.5 hr over which the ambient seismic data were collected. The other seismic sources in the *ZZ* model can not explain the C_{RR} waveforms. Thus the *ZZ* + *RR* inversion provides a better result than the *ZZ* inversion. We also note that the *ZZ* + *RR* inversion required one less iteration than the *ZZ* inversion and from previous work (Xu *et al.* 2019) we know that *RR* data have better resolution than *ZZ* data when the SNR of the two data are comparable.

4 DISCUSSION

It is important to estimate the uncertainty in inversion problems. Uncertainty in inversion results is due to (1) errors in data, (2) errors in the physics and (3) insufficient sensitivity (resolution) of the inverse problem based on the spatial data sampling. We focus on the latter two here, noting that it is difficult to assess the true uncertainty in the source waveform inversion. For instance, we have incorporated smoothing, a type of regularization, into the inversion. Thus any estimated uncertainty would be for the regularized solution rather than for the true solution (e.g. Aster *et al.* 2011). To address the issue of uncertainty one could use Monte Carlo methods (e.g. Sen & Stoffa 1991; Tarantola 2005) because one does not necessary need to adopt a regularization.

4.1 Inaccurate velocity model

We make two major assumptions in the waveform inversion method (listed in Section 1), and any violation of these assumptions leads to errors in the physics of the inverse problem. Here we consider the first assumption (that the subsurface structure is known) and focus on the error due to (i) an inaccurate subsurface velocity model or (ii) using an incorrect material model (e.g. elastic versus anelastic).

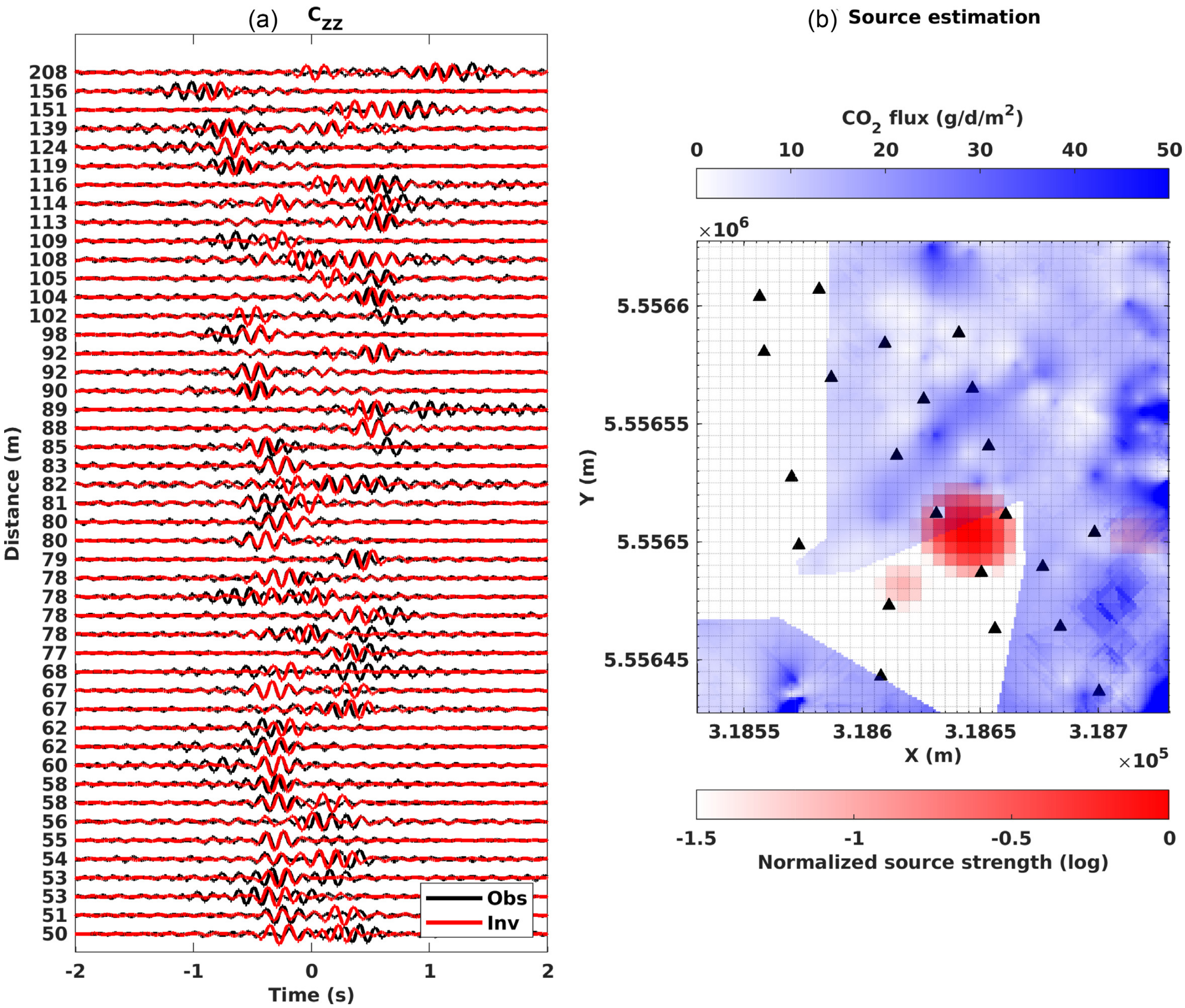

Figure 7. The data comparison and source distribution map from the inversion of C_{ZZ} waveforms. (a) The observed and synthetic C_{ZZ} waveforms are arranged based on the interstation distance of sensor pairs. Each waveform is bandpass filtered between 4.5 and 9 Hz and then normalized by its maximum amplitude for visual comparison. (b) The red area indicates the seismic source area and the red colour indicates the source strength. The blue colour indicates measured CO$_2$ gas fluxes in the unit of gram per day per metre square (Nickschick *et al.* 2015). Black triangles are the geophones. The coordinates are in WGS84/UTM, zone 33.

First, inaccurate velocity models are known to lead to artefacts and biased source location in traditional source imaging methods (e.g. Billings *et al.* 1994; Eisner *et al.* 2009). In full-waveform inversion (FWI), one can not resolve a source distribution accurately with an inaccurate velocity model because the two are coupled within the misfit function (e.g. Fichtner 2015). Here we have neglected that coupling, but Xu *et al.* (2019) study the source waveform inversion using an incorrect elastic velocity model and find that this increases the misfit and moves the estimated source location. In the field data presented here, we assume that the subsurface is laterally homogeneous and elastic, but the real subsurface is laterally heterogeneous and anelastic (e.g. Nickschick *et al.* 2015).

The second violation we must consider is related to an anelastic material. We know that wave propagation through anelastic media influences the array sensitivity because, due to attenuation, some stations may not record signal from a given source. Therefore, different stations will sense different sources, potentially leading to competing source models within the inverse problem. Therefore, we study the effect of the anelasticity on the source waveform inversion here. Similar to the synthetic tests (Section 3.1), we generate synthetic data with an anelastic model to use as the observed data. From these data we estimate the incorrect S_Z^0 and S_R^0, and then apply the source waveform inversion using an elastic model. In doing so, we make the assumption that the observed data are elastic, directly leading to a violation of the inverse problem physics.

To generate anelastic data, we use anelastic Rayleigh-wave Green's functions:

$$G_{ZZ}^{\alpha}(r,\omega) = \sqrt{\frac{1}{8\pi\omega r/c}}\,\mathrm{e}^{-i(\omega r/c+\pi/4)}\mathrm{e}^{-\alpha r}, \tag{16}$$

and

$$G_{RZ}^{\alpha}(r,\omega) = \frac{H(\omega)}{V(\omega)}\sqrt{\frac{1}{8\pi\omega r/c}}\,\mathrm{e}^{-i(\omega r/c-\pi/4)}\mathrm{e}^{-\alpha r}, \tag{17}$$

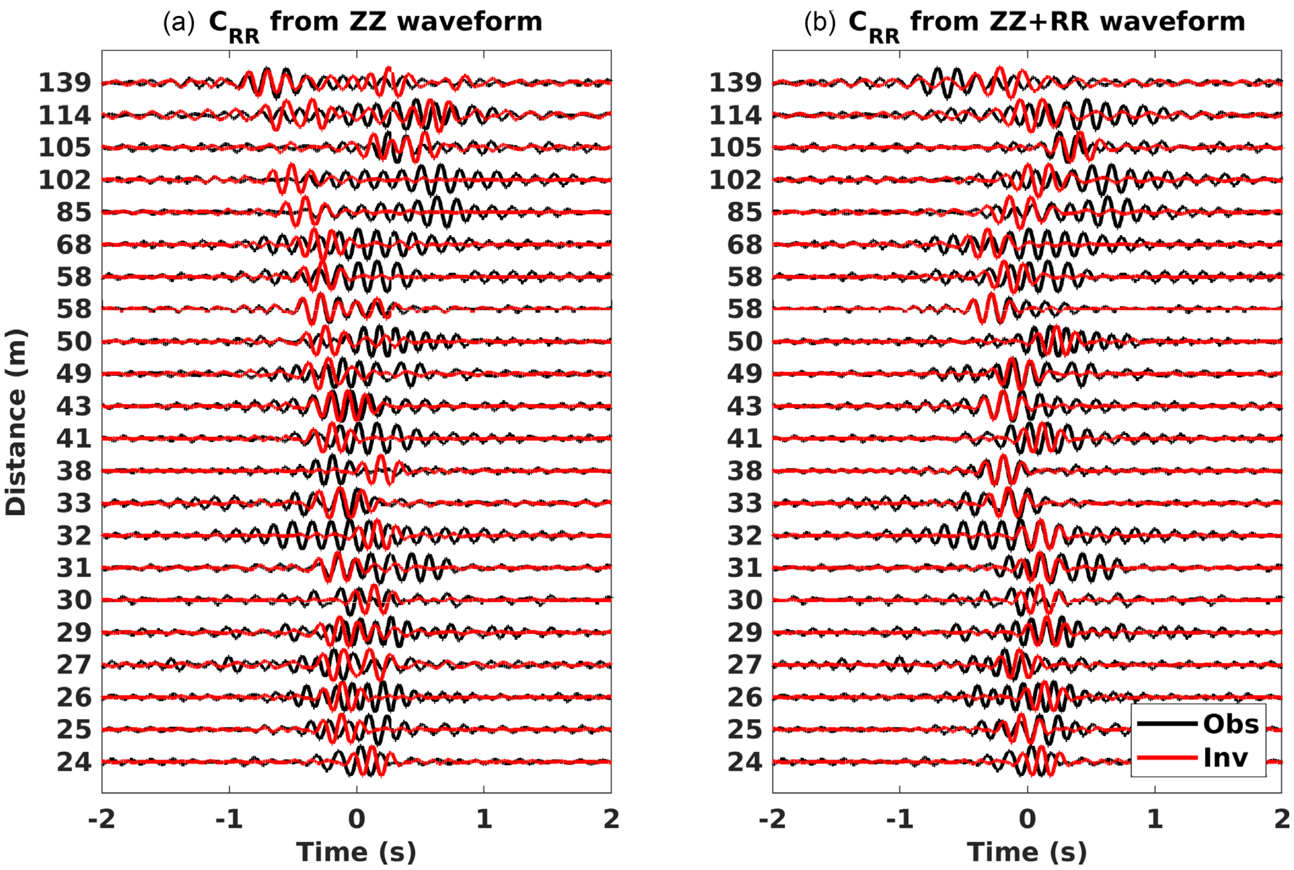

Figure 8. The C_{RR} waveform comparisons from the inversion of *ZZ* (a) and *ZZ* + *RR* (b) crosscorrelations.

where α is the attenuation coefficient for Rayleigh waves (e.g. Lai *et al.* 2002; Xia *et al.* 2002). We use $\alpha = 0.01\omega/2\pi$ here. For the source energy spectral density estimation, our estimations of S_Z^0 and S_R^0 from the anelastic observed data autocorrelations (blue lines in Fig. 5) are biased and should be corrected (e.g. Groos *et al.* 2014) if possible. This bias is because our estimation procedure is based on an elastic medium and does not compensate the amplitude loss due to the anelastic attenuation, $e^{-\alpha r}$ in eqs (16) and (17). Here we do not correct this bias in order to assess the significance of this violation on the two-source example. We use the biased source energy spectral density estimates in the source waveform inversion, and observe that in all cases the misfits for the anelastic data are larger than the elastic model results (Table 1). The non-smoothed *ZZ* and *ZZ* + *RR* anelastic data inversion results are similar to each other (Figs 6g and i), and both models only resolve one source instead of two. Thus the anelasticity can lead to missed sources, and in this case the one-source model is likely due to the interstation crosscorrelation coverage (Figs 6a and b), which largely samples the one source that is resolved. Thus, in the case of anelastic data, one should use an anelastic model (e.g. Groos *et al.* 2014, 2017).

We apply the above test to a model with one out-of-array source. This source is in a similar location as the estimated source from the field *ZZ* + *RR* data (Fig. 9b). The synthetic observed data come from the anelastic model, and we use the elastic model in the inversion. We observe that the *ZZ* inversion images spurious strong sources in the array and a weak source in the true source area (Fig. 10a). In contrast, the *ZZ* + *RR* inversion accurately estimates the true source location (Fig. 10b). This observation indicates that even when the source inversion uses an elastic model, but the observed data come from an anelastic model, the multicomponent data provide a more accurate source estimation than the vertical-component data alone. Regardless of the lost resolution due to smoothing the kernels, this highlights the usefulness of incorporating the multicomponent crosscorrelations into source waveform inversion.

The last point to note related to violating the physics is that the subsurface velocity model changes when the CO_2 gas is moving through the subsurface and escaping into the atmosphere (e.g. Ikeda *et al.* 2016). Thus it is likely necessary to jointly estimate both the source distribution and subsurface velocity models from ambient seismic noise data either iteratively or simultaneously (e.g. Sager *et al.* 2018) to get the most accurate results. This is an area of future research and we plan to work on a joint inversion in the future.

4.2 Insufficient sensitivity

Besides attenuation, insufficient sensitivity in the inverse problem is due to the array geometry and the sensor pairs we choose based on the SNR of the crosscorrelations. The array geometry can lead to a null space in the inverse problem and thus there is zero sensitivity to sources located in a particular region of the model. To determine how significant the errors are in the final results, one could do synthetic tests to characterize how the source location and strength changes with array geometry. Xu *et al.* (2019) study sources inside the array and outside of the array and find that sources outside of the array are smeared due to the lack of resolution.

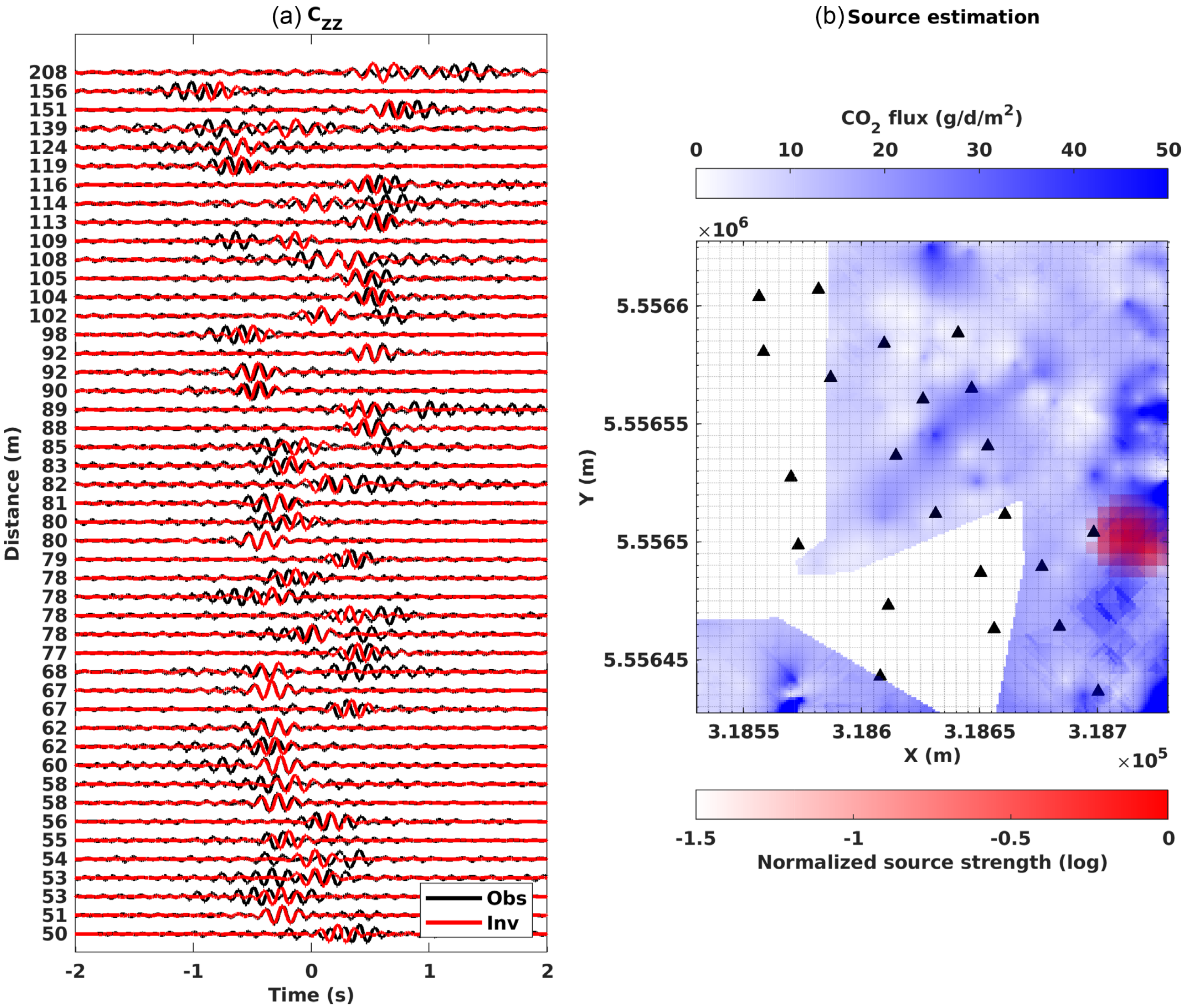

Figure 9. The data comparison and source distribution map from the inversion of C_{ZZ} and C_{RR} waveforms. All inversion parameters match those in Fig. 7.

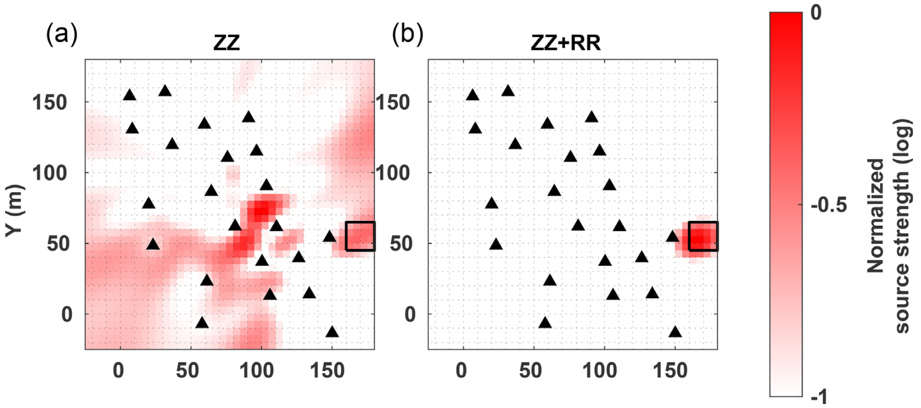

Figure 10. The anelastic synthetic data inversion results for one out-of-array source. The true source strength is zero everywhere except for the out-of-array source area which is indicated by the empty box. We invert ZZ and $ZZ + RR$ waveforms with smoothing (a and b, respectively). All inversion parameters match those in Fig. 6.

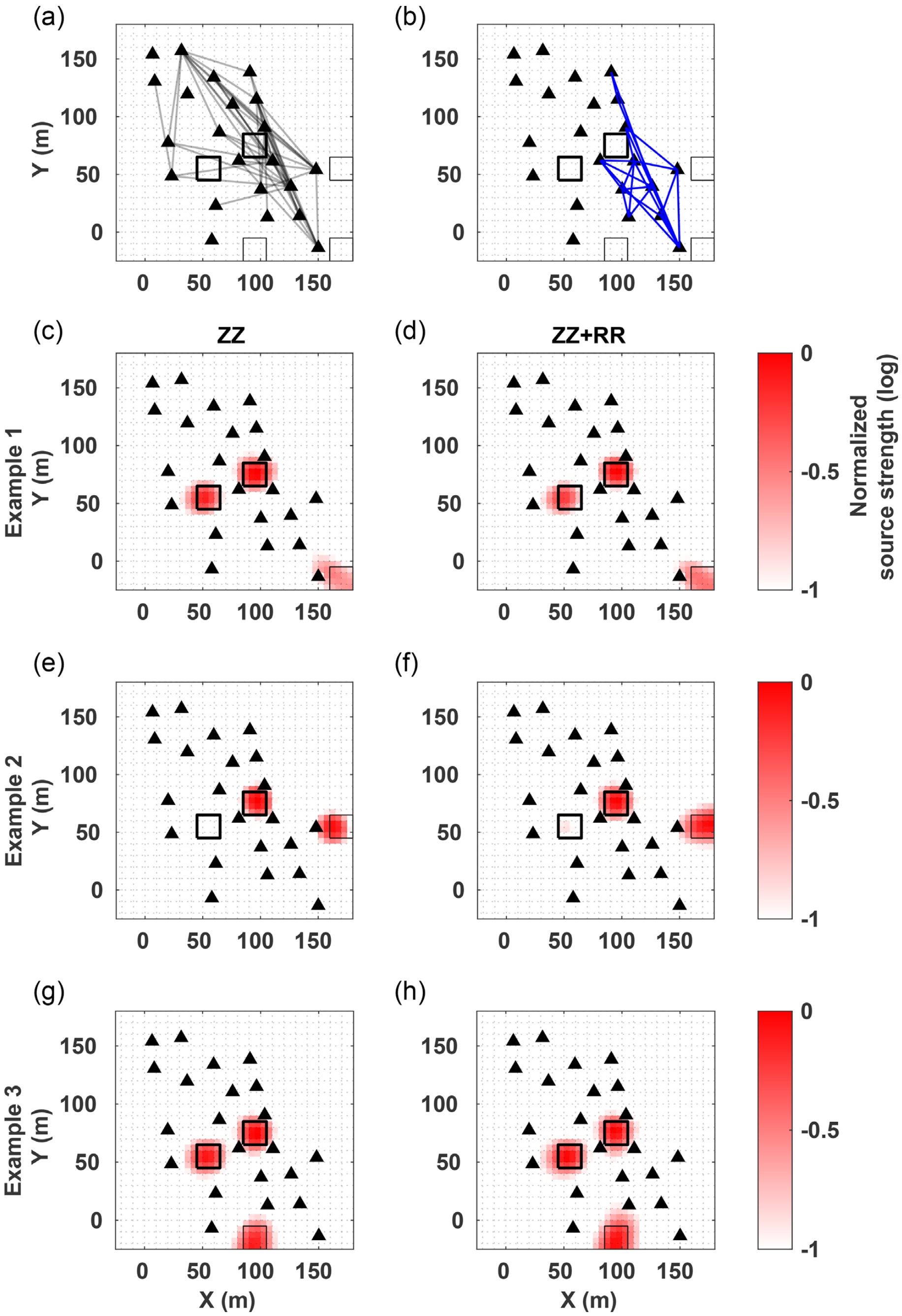

Figure 11. The three out-of-array source inversion results. The true source strength is zero everywhere except for the two fixed sources within the array and the one moving source outside of the array. The sources are represented by empty black squares. The initial inversion model is that in Fig. 6(b). For the elastic model crosscorrelations, we invert the *ZZ* waveforms (c, e, g) and *ZZ* + *RR* waveforms (d, f, h). We use the same sensor pairs as in Fig. 6: 47 C_{ZZ} sensor pairs (grey lines in a) and 22 C_{RR} sensor pairs (blue lines in b).

To study the relationship between in- and out-of-array sources here, we complete a third synthetic elastic test. We add an out-of-array source region to our previous two-source synthetic elastic model (Fig. 6) at three different locations. On the one hand, we observe that the waveform inversion resolves the out-of-array source, but with a reduced amplitude compared to the in-array sources (Fig. 11), even though the true amplitudes for all the sources are the same. On the other hand, the waveform inversion may resolve out-of-array sources in biased locations when only the *ZZ* waveforms are used (Fig. 11e). This is in contrast to the *ZZ* + *RR* inversion, which resolves the sources more accurately than the *ZZ* inversion (Fig. 11f) in this numerical experiment. Thus, although we have shown that the *ZZ* and *ZZ* + *RR* inversions result in similar models and misfits after applying regularization (i.e. smoothing), we recommend using all possible data in order to image sources as accurately as possible. We note that we have not tried more than three sources in our testing up to now.

In practice, seismic waves from out-of-array sources will be attenuated due to the anelasticity in the subsurface. The attenuated wave amplitude may be masked by random noise. Therefore the anelasticity can also decrease the source resolution on out-of-array sources. This research area deserves further studies but is not the focus of our study.

5 CONCLUSION

We present a complete workflow to estimate the seismic source distribution from ambient seismic noise data. In the workflow, we propose an SNR measurement and apply a SNR criterion to select high-quality seismic crosscorrelations. We determine that it is important to select time windows that contribute to the overall SNR of the array, and to exclude untargeted seismic sources from the crosscorrelations. Under the assumption that the subsurface is elastic and laterally homogeneous, we estimate the Green's functions and develop a novel algorithm to retrieve the source energy spectral density. Finally, we apply the waveform inversion to the highest quality crosscorrelations of field data and synthetic data sets using the same receiver geometries. We determine that $ZZ + RR$ better constrains the seismic source distribution than ZZ in elastic medium, and for anelastic data both $ZZ + RR$ and ZZ fail to recognize all seismic sources. The field data inversion results indicate a strong seismic source near the strong CO_2 gas flux area. The workflow presented is applicable for both vertical and multicomponent data, and also different scale field data.

ACKNOWLEDGEMENTS

ZX thanks Scott Burdick for fruitful discussions. JU thanks Prof Dr Michael Korn for his supervision. The authors thank editor Dr M.H. Ritzwoller, Dr Sidao Ni and two anonymous reviewers for their constructive feedback that helped improve this manuscript. The authors also thank Tobias Nickschick for providing the CO_2 gas flux data. The seismic data acquisition in Hartoušov and JU were funded by the Deutsche Forschungsgemeinschaft (DFG) in the framework of SPP-1006. This research is supported by the National Science Foundation under Grant No. 1643795.

REFERENCES

Ardhuin, F., Stutzmann, E., Schimmel, M. & Mangeney, A., 2011. Ocean wave sources of seismic noise, *J. geophys. Res.,* **116**(C9), doi:10.1029/2011JC006952.

Aster, R.C., Borchers, B. & Thurber, C.H., 2011. *Parameter Estimation and Inverse Problems,* Vol. **90,** Academic Press.

Bensen, G.D., Ritzwoller, M.H., Barmin, M.P., Levshin, A.L., Lin, F., Moschetti, M.P. & Yang, Y., 2007. Processing seismic ambient noise data to obtain reliable broad-band surface wave dispersion measurements, *J. geophys. Int.,* **169**(3), 1239–1260.

Billings, S., Sambridge, M. & Kennett, B., 1994. Errors in hypocenter location: picking, model, and magnitude dependence, *Bull. seism. Soc. Am.,* **84**(6), 1978–1990.

Bozdağ, E., Trampert, J. & Tromp, J., 2011. Misfit functions for full waveform inversion based on instantaneous phase and envelope measurements, *J. geophys. Int.,* **185**(2), 845–870.

Bussert, R. *et al.*, 2017. Drilling into an active mofette: pilot-hole study of the impact of CO_2-rich mantle-derived fluids on the geo–bio interaction in the western Eger Rift (Czech Republic), *Sci. Drilling,* **23,** 13.

Cessaro, R.K., 1994. Sources of primary and secondary microseisms, *Bull. seism. Soc. Am.,* **84**(1), 142–148.

Cheng, F., Xia, J., Xu, Y., Xu, Z. & Pan, Y., 2015. A new passive seismic method based on seismic interferometry and multichannel analysis of surface waves, *J. appl. Geophys.,* **117,** 126–135.

Cheng, F. *et al.*, 2016. Multi-channel analysis of passive surface waves based on cross-correlations, *Geophysics,* **81**(5), EN57–EN66.

Corciulo, M., Roux, P., Campillo, M., Dubucq, D. & Kuperman, W., 2012. Multiscale matched-field processing for noise-source localization in exploration geophysics, *Geophysics,* **77**(5), KS33–KS41.

Cros, E., Roux, P., Vandemeulebrouck, J. & Kedar, S., 2011. Locating hydrothermal acoustic sources at Old Faithful Geyser using matched field processing, *J. geophys. Int.,* **187**(1), 385–393.

Delaney, E., Ermert, L., Sager, K., Kritski, A., Bussat, S. & Fichtner, A., 2017. Passive seismic monitoring with nonstationary noise sources, *Geophysics,* **82**(4), KS57–KS70.

Eisner, L., Duncan, P.M., Heigl, W.M. & Keller, W.R., 2009. Uncertainties in passive seismic monitoring, *Leading Edge,* **28**(6), 648–655.

Ermert, L., Villaseñor, A. & Fichtner, A., 2015. Cross-correlation imaging of ambient noise sources, *J. geophys. Int.,* **204**(1), 347–364.

Ermert, L., Sager, K., Afanasiev, M., Boehm, C. & Fichtner, A., 2017. Ambient seismic source inversion in a heterogeneous Earth-Theory and application to the Earth's hum, *J. geophys. Res.,* **122**(11), 9184–9207.

Estrella, H.F., Umlauft, J., Schmidt, A. & Korn, M., 2016. Locating mofettes using seismic noise records from small dense arrays and matched field processing analysis in the NW Bohemia/Vogtland Region, Czech Republic, *Near Surf. Geophys.,* **14**(4), 327–335.

Fichtner, A., 2015. Source-structure trade-offs in ambient noise correlations, *J. geophys. Int.,* **202**(1), 678–694.

Fichtner, A., Kennett, B.L., Igel, H. & Bunge, H.-P., 2008. Theoretical background for continental-and global-scale full-waveform inversion in the time–frequency domain, *J. geophys. Int.,* **175**(2), 665–685.

Fichtner, A., Stehly, L., Ermert, L. & Boehm, C., 2017. Generalised interferometry—I. Theory for inter-station correlations, *J. geophys. Int.,* **208,** 603–638.

Groos, L., Schäfer, M., Forbriger, T. & Bohlen, T., 2014. The role of attenuation in 2D full-waveform inversion of shallow-seismic body and Rayleigh waves, *Geophysics,* **79**(6), R247–R261.

Groos, L., Schäfer, M., Forbriger, T. & Bohlen, T., 2017. Application of a complete workflow for 2D elastic full-waveform inversion to recorded shallow-seismic Rayleigh waves, *Geophysics,* **82**(2), R109–R117.

Haney, M.M., Mikesell, T.D., van Wijk, K. & Nakahara, H., 2012. Extension of the spatial autocorrelation (SPAC) method to mixed-component correlations of surface waves, *J. geophys. Int.,* **191**(1), 189–206.

He, Y., Monahan, A.H. & McFarlane, N.A., 2013. Diurnal variations of land surface wind speed probability distributions under clear-sky and low-cloud conditions, *Geophys. Res. Lett.,* **40**(12), 3308–3314.

Ikeda, T., Tsuji, T., Watanabe, T. & Yamaoka, K., 2016. Development of surface-wave monitoring system for leaked CO_2 using a continuous and controlled seismic source, *Int. J. Greenhouse Gas Contl.,* **45,** 94–105.

Johansen, H., 1977. A man/computer interpretation system for resistivity soundings over a horizontally strafified earth, *Geophys. Prospect.,* **25**(4), 667–691.

Juretzek, C. & Hadziioannou, C., 2016. Where do ocean microseisms come from? A study of Love-to-Rayleigh wave ratios, *J. geophys. Res.,* **121**(9), 6741–6756.

Kennett, B.L., Engdahl, E. & Buland, R., 1995. Constraints on seismic velocities in the Earth from traveltimes, *J. geophys. Int.,* **122**(1), 108–124.

Lai, C.G., Rix, G.J., Foti, S. & Roma, V., 2002. Simultaneous measurement and inversion of surface wave dispersion and attenuation curves, *Soil Dyn. Earthq. Eng.,* **22**(9-12), 923–930.

Lin, F., Moschetti, M.P. & Ritzwoller, M.H., 2008. Surface wave tomography of the western United States from ambient seismic noise: Rayleigh and Love wave phase velocity maps, *J. geophys. Int.,* **173**(1), 281–298.

Lin, F.-C., Li, D., Clayton, R.W. & Hollis, D., 2013. High-resolution 3D shallow crustal structure in Long Beach, California: application of ambient noise tomography on a dense seismic array, *Geophysics,* **78**(4), Q45–Q56.

Luo, Y., Yang, Y., Xu, Y., Xu, H., Zhao, K. & Wang, K., 2015. On the limitations of interstation distances in ambient noise tomography, *J. geophys. Int.,* **201**(2), 652–661.

Maggi, A., Tape, C., Chen, M., Chao, D. & Tromp, J., 2009. An automated time-window selection algorithm for seismic tomography, *J. geophys. Int.,* **178**(1), 257–281.

McMechan, G.A. & Yedlin, M.J., 1981. Analysis of dispersive waves by wave field transformation, *Geophysics,* **46**(6), 869–874.

Mikesell, T.D., van Wijk, K., Calvert, A. & Haney, M.M., 2009. The virtual refraction: useful spurious energy in seismic interferometry, *Geophysics,* **74**(3), A13, doi:10.1190/1.3095659.

Nakata, N., Chang, J.P., Lawrence, J.F. & Boué, P., 2015. Body wave extraction and tomography at Long Beach, California, with ambient-noise interferometry, *J. geophys. Res.,* **120**(2), 1159–1173.

Nickschick, T., Kämpf, H., Flechsig, C., Mrlina, J. & Heinicke, J., 2015. CO_2 degassing in the Hartoušov mofette area, western Eger Rift, imaged by CO_2 mapping and geoelectrical and gravity surveys, *Int. J. Earth Sci.,* **104**(8), 2107–2129.

Obara, K., 2002. Nonvolcanic deep tremor associated with subduction in southwest Japan, *Science,* **296**(5573), 1679–1681.

Park, C.B., Miller, R.D., Xia, J. *et al.*, 1998. Imaging dispersion curves of surface waves on multi-channel record, in *SEG Technical Program Expanded Abstracts 1998,* pp. 1377–1380, SEG.

Roux, P. *et al.*, 2018. Toward seismic metamaterials: the METAFORET project, *Seismol. Res. Lett.,* **89**(2A), 582–593.

Sager, K., Ermert, L., Boehm, C. & Fichtner, A., 2018. Towards full waveform ambient noise inversion, *J. geophys. Int.,* **212**(1), 566–590.

Sager, K., Boehm, C., Ermert, L., Krischer, L. & Fichtner, A., 2020. Global-scale full-waveform ambient noise inversion, *J. geophys. Res.,* **125**(4), doi:10.1029/2019JB018644.

Schimmel, M. & Paulssen, H., 1997. Noise reduction and detection of weak, coherent signals through phase-weighted stacks, *J. geophys. Int.,* **130**(2), 497–505.

Sen, M.K. & Stoffa, P.L., 1991. Nonlinear one-dimensional seismic waveform inversion using simulated annealing, *Geophysics,* **56**(10), 1624–1638.

Shapiro, N.M., Michel, C., Laurent, S. & Ritzwoller, M.H., 2005. High-resolution surface-wave tomography from ambient seismic noise, *Science,* **307,** 1615–1618.

Shapiro, N.M., Ritzwoller, M. & Bensen, G., 2006. Source location of the 26 sec microseism from cross-correlations of ambient seismic noise, *Geophys. Res. Lett.,* **33**(18), doi:10.1029/2006GL027010.

Snieder, R. & Fleury, C., 2010. Cancellation of spurious arrivals in Green's function retrieval of multiple scattered waves, *J. acoust. Soc. Am.,* **128**(4), 1598–1605.

Takano, T., Brenguier, F., Campillo, M., Peltier, A. & Nishimura, T., 2019. Noise-based passive ballistic wave seismic monitoring on an active volcano, *J. geophys. Int.,* **220**(1), 501–507.

Tape, C., Liu, Q. & Tromp, J., 2007. Finite-frequency tomography using adjoint methods–Methodology and examples using membrane surface waves, *J. geophys. Int.,* **168**(3), 1105–1129.

Tarantola, A., 2005. *Inverse Problem Theory and Methods for Model Parameter Estimation,* Vol. **89,** SIAM, doi:10.1137/1.9780898717921.

Tian, Y. & Ritzwoller, M.H., 2015. Directionality of ambient noise on the Juan de Fuca plate: Implications for source locations of the primary and secondary microseisms, *J. geophys. Int.,* **201**(1), 429–443.

Tromp, J., Luo, Y., Hanasoge, S. & Peter, D., 2010. Noise cross-correlation sensitivity kernels, *J. geophys. Int.,* **183**(2), 791–819.

Tsai, V.C., Minchew, B., Lamb, M.P. & Ampuero, J.-P., 2012. A physical model for seismic noise generation from sediment transport in rivers, *Geophys. Res. Lett.,* **39**(2), doi:10.1029/2011GL050255.

Umlauft, J. & Korn, M., 2019. 3-D fluid channel location from noise tremors using matched field processing, *J. geophys. Int.,* **219**(3), 1550–1561.

Wang, L., Xu, Y. & Luo, Y., 2015. Numerical Investigation of 3D multichannel analysis of surface wave method, *J. appl. Geophys.,* **119,** 156–169.

Xia, J., Miller, R.D., Park, C.B. & Tian, G., 2002. Determining Q of near-surface materials from Rayleigh waves, *J. appl. Geophys.,* **51**(2-4), 121–129.

Xu, Z. & Mikesell, T.D., 2017. On the reliability of direct Rayleigh-wave estimation from multicomponent cross-correlations, *J. geophys. Int.,* **210**(3), 1388–1393.

Xu, Z., Mikesell, T.D., Xia, J. & Cheng, F., 2017. A comprehensive comparison between the refraction microtremor and seismic interferometry methods for phase-velocity estimation, *Geophysics,* **82**(6), EN99–EN108.

Xu, Z., Mikesell, T.D., Gribler, G. & Mordret, A., 2019. Rayleigh-wave multicomponent crosscorrelation-based source strength distribution inversion. Part 1: theory and numerical examples, *J. geophys. Int.,* **218**(3), 1761–1780.

Yamanaka, H., Dravinski, M. & Kagami, H., 1993. Continuous measurements of microtremors on sediments and basement in Los Angeles, California, *Bull. seism. Soc. Am.,* **83**(5), 1595–1609.

Yang, Y. & Ritzwoller, M.H., 2008. Characteristics of ambient seismic noise as a source for surface wave tomography, *Geochem. Geophys. Geosyst.,* **9**(2), 1256–1256.

Yao, H. & van Der Hilst, R.D., 2009. Analysis of ambient noise energy distribution and phase velocity bias in ambient noise tomography, with application to SE Tibet, *J. geophys. Int.,* **179**(2), 1113–1132.

Zeng, X. & Ni, S., 2010. A persistent localized microseismic source near the Kyushu Island, Japan, *Geophys. Res. Lett.,* **37**(24), doi:10.1029/2010GL045774.

van Wijk, K., Mikesell, T. D., Schulte-Pelkum, V. & Stachnik, J., 2011. Estimating the Rayleigh-wave impulse response between seismic stations with the cross terms of the Green tensor , *Geophys. Res. Lett.,* **38,** 16. https://doi.org/10.1029/2011GL047442.

SUPPORTING INFORMATION

Supplementary data are available at *GJI* online.

Figure S1. The number of sensor pairs with SNR>15 changes with time as we stack more time sections of crosscorrelations. The dashed lines are the same as in Fig. 3. The solid lines are the SNR results if we skip the seismic recordings between 03:30 and 03:35. The time axis is from 01:00 to 05:00 on 23 November 2016.

Figure S2. The source distribution maps from MFP, the ZZ and ZZ+RR inversions. We apply the MFP to the high-SNR C_{ZZ} and all C_{ZZ} waveforms between 4.5 and 9 Hz to estimate MFP source models (a and b, respectively). We then use the MFP result as the initial model in the ZZ and ZZ+RR inversions (c and d). The inversion parameters are the same as in Section 3.

Figure S3. The normalized misfits from the inversion of the field data. We show the misfits over the whole frequency band, 4.5–9 Hz, relative to the initial misfit at each iteration. The dashed lines indicate the inversion results using the MFP initial model, while the solid lines indicate the results using the initial model presented in Section 3.

Figure S4. The seismic recordings across the 22 sensors between 146.3 and 146.5 minute (02:26). The recordings are filtered between 4.5 and 9 Hz in the frequency. The two red dash lines indicate a velocity of 200 m s^{-1}. The traces are plotted relative to the source–receiver offset using the inverted source location in Fig. 9(b).

APPENDIX A: SOURCE KERNELS

We compare the *ZZ* and *RR* source sensitivity kernels for two different interstation distances, 20 and 100 m. Although some previous studies discussed the interstation distances (e.g. Bensen *et al.* 2007; Luo *et al.* 2015), these studies are for ANT not for source estimation. Furthermore, these studies did not consider the source sensitivity kernels. Thus it is still necessary to discuss the effect of different interstation distance on the source sensitivity kernels.

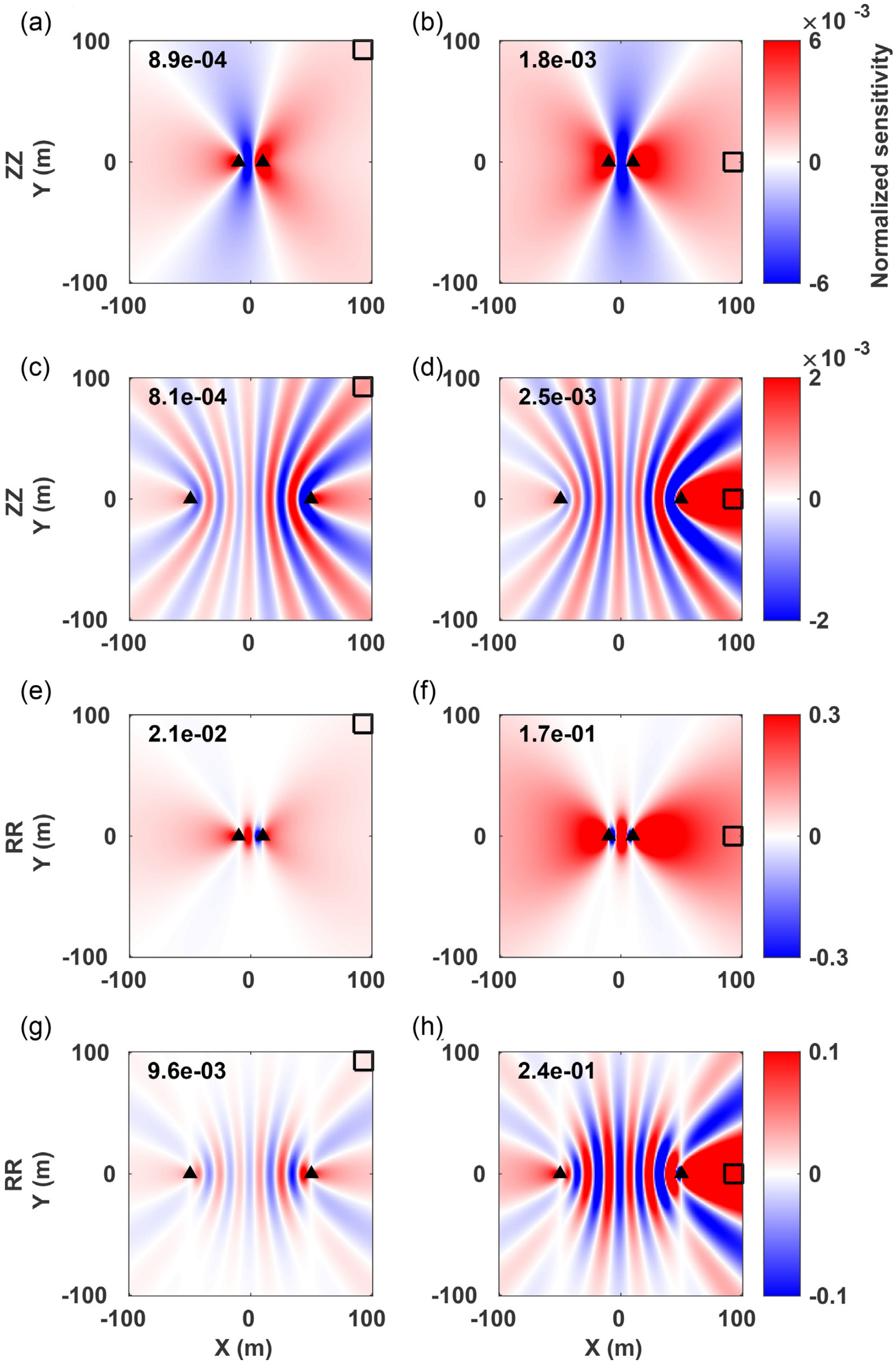

Figure A1. *ZZ* and *RR* waveform energy source sensitivity kernels for out-of-line (left-hand column) and in-line (right-hand column) initial source models. The two sensors are separated by 20 m (a, b, e and f) and 100 m (c, d, g and h). All the sensitivity kernels are normalized by the absolute maximum value in (e). The black triangles are sensors. The black empty squares indicate the source locations. In each subplot, the number in the top left-hand corner indicates the sensitivity value in the center of the square. We calculate the kernels from 4.5 to 6 Hz and use the same Green's functions and S_Z^0 (S_R^0) as in the paper.

We set the observed data be zeros (eq. 10) and focus on the synthetic waveform energy in the time window –2 to 2 s. We examine two initial source cases: (i) an out-of-line source (small black box in upper right of Figs A1a, c, e, g) and (ii) an in-line source (small black box on center right of Figs A1b, d, f, h). From these initial distributions, we calculate synthetic crosscorrelations using the forward model (eq. 11). The 20 m interstation distance synthetic C_{ZZ} waveforms are similar for the two source cases (Fig. A2a), while the 20 m C_{RR} waveforms have significantly different amplitudes (Fig. A2b). For the 100 m sensor pair, the C_{ZZ} waveforms are quite different for the two source cases (Fig. A2c), as are the C_{RR} waveforms (Fig. A2d) indicating that these crosscorrelations are more sensitive to the source distribution than the small station spacing crosscorrelations.

From the waveforms, we can calculate source sensitivity kernels (eq. 13). The sensitivity kernels indicate how source strength

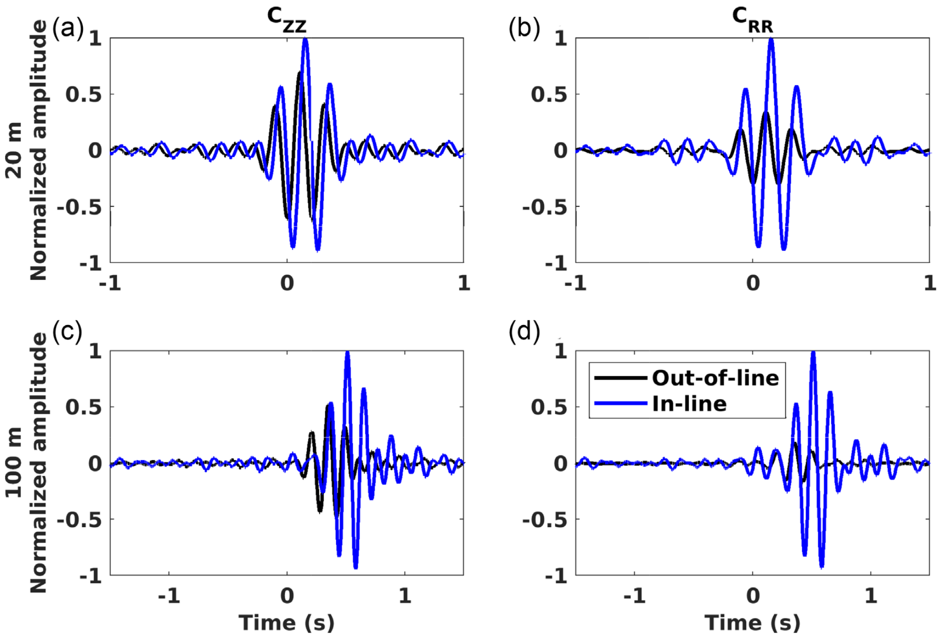

Figure A2. Comparison of synthetic C_{ZZ} and C_{RR} waveforms between the in-line and out-of-line source cases. The top row is for the 20 m interstation distance sensor pair; the bottom row is for the 100 m interstation distance sensor pair. Each waveform is bandpass filtered between 4.5 and 9 Hz and then normalized by the maximum amplitude of the in-line crosscorrelations so that relative amplitudes are preserved.

changes affect the synthetic waveform energy. We observe that the first Fresnel zone in the source sensitivity kernels for the 20 m sensor pair (Figs A1a, b, e and f) is much larger than for the 100 m sensor pair (Figs A1c, d, g and h). For the small-distance sensor pair, the *ZZ* sensitivity kernels are similar when the initial source location changes (Figs A1a and b), while the *RR* sensitivity kernels change more dramatically with initial source distribution (Figs A1e and f); the two *ZZ* sensitivity values in the source locations are the same order (a factor of 2 different) while the in-line *RR* sensitivity values are almost an order of magnitude different (a factor of 10) than the out-of-line source. This variation in sensitivity is because of the azimuthal effect of the *R* component (e.g. van Wijk et al. 2011; Haney *et al.* 2012; Xu & Mikesell 2017; Xu *et al.* 2019). Thus, incorporating multicomponent crosscorrelations into the FWI provides additional sensitivity that helps resolve sources, even when the station spacing is small. While we recognize that the RR kernels provide important azimuthal information for the inversion, we have not fully characterized the degree to which station-pair azimuth sampling plays a role in the inversion, and this is one topic of future research.

APPENDIX B: CALCULATING RAYLEIGH-WAVE PHASE VELOCITIES

We estimate the phase velocity by combining classic ambient seismic noise processing (e.g. Bensen *et al.* 2007) and surface wave velocity analysis (e.g. McMechan & Yedlin 1981; Park *et al.* 1998). In order to calculate accurate surface wave phase velocities, one needs to mitigate the effects of an anisotropic source distribution by using long recordings and/or time-/frequency-domain normalization (e.g. Yang & Ritzwoller 2008). Here we use 2 days of geophone recordings (22 and 23 November 2016). We divide the data into 60 s sections and remove the mean and linear trend from each section. We then apply one-bit amplitude normalization to the sections, crosscorrelate, and linearly stack. Note that we focus on accurate Rayleigh-wave phase velocities, not waveforms. Thus we use the one-bit time-domain normalization procedure.

We stack all of the crosscorrelations into 1 m offset bins to generate a virtual shot gather (Figs B1a and b). We sum the causal and acausal parts of the gather and then create a dispersion image (Figs B1c and d) by applying the phase-shift velocity transform (Park *et al.* 1998). We observe a clear Rayleigh-wave dispersion signal in the C_{ZZ} waveforms (Fig. B1c). We pick the Rayleigh-wave phase velocity based on the maximum of coherence every 0.5 Hz in the 3–10 Hz band and smooth the phase velocities with an average window (black line in Fig. B1c). Although the dispersion trend is continuous, these phase velocities can still be biased due to an anisotropic seismic source distribution (e.g. Yang & Ritzwoller 2008; Yao & van Der Hilst 2009; Xu *et al.* 2017). We examine the accuracy of the phase velocities in a qualitative way by comparing the C_{ZZ}-derived phase velocity (the black line in Fig. B1d) to the dispersion trend from C_{RR} (Fig. B1d). C_{RR} is less sensitive to anisotropic seismic source distributions (e.g. Xu & Mikesell 2017). In the dispersion image (Fig. B1d), we observe that the phase velocities from C_{ZZ} are close to C_{RR} in the 4–10 Hz band. This similarity indicates that the phase velocities are reliable. Knowing that this dispersion estimation is an average phase velocity for the subsurface (e.g. Wang *et al.* 2015), we use this dispersion estimation in the analytical Green's functions (eqs 1 and 2).

APPENDIX C: CONVERTING VELOCITY RECORDINGS TO DISPLACEMENT RECORDINGS

The geophones in this study recorded the ground motion velocity at the geophone locations, while the Green's functions (eqs 1 and 2) are the displacement Green's functions instead of the velocity Green's functions. Based on the Fourier transform, there is a ratio $i\omega$ that relates the spectra of velocity recordings (V) and the displacement

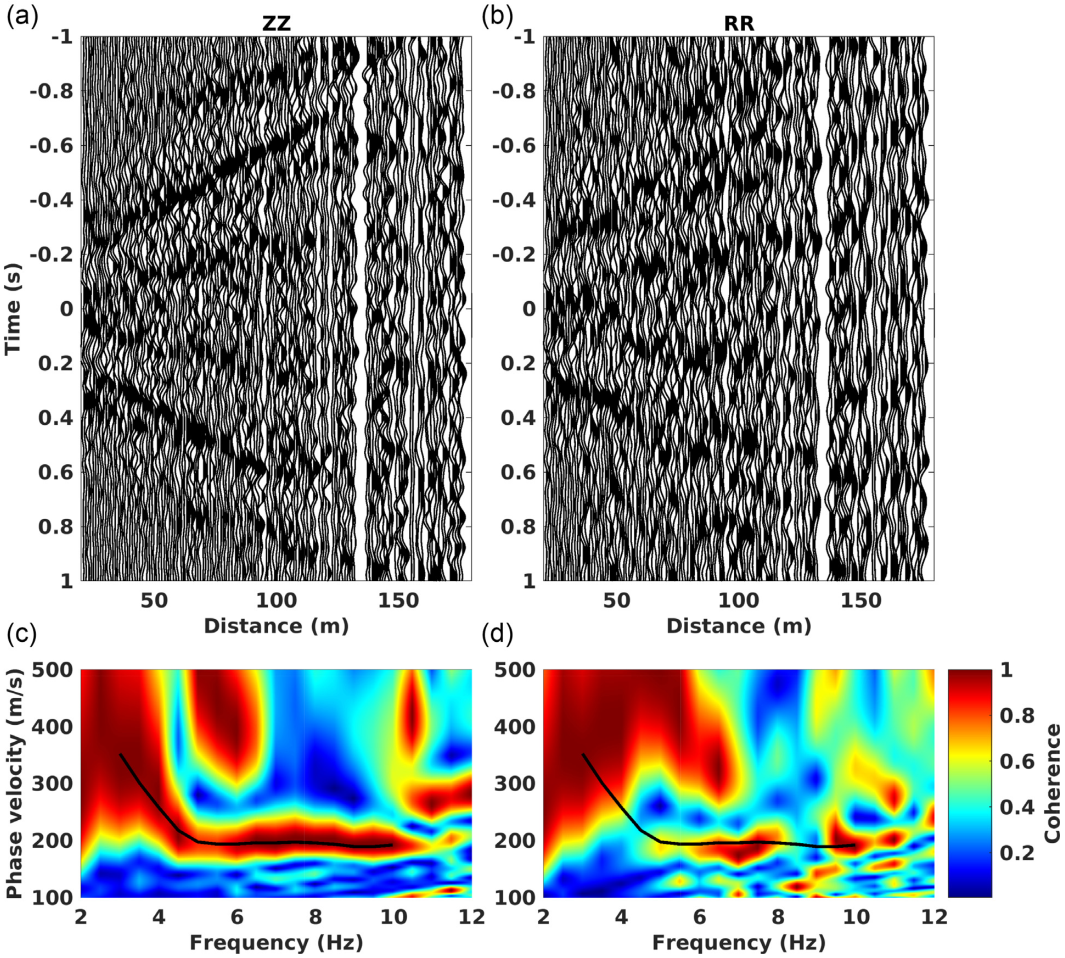

Figure B1. The virtual shot gathers of C_{ZZ} (a) and C_{RR} (b) after applying a 1 m bin-stack to all crosscorrelations. We apply the phase-shift transform to the sum of causal and acausal parts of the crosscorrelations to generate the dispersion images (c and d). The black lines in the two dispersion images are the smoothed phase velocities from C_{ZZ}. The waveforms are band-pass filtered between 2 and 12 Hz.

recordings (U):

$$V = i\omega U. \qquad \text{(C1)}$$

For crosscorrelations this relationship becomes

$$VV^* = \omega^2 UU^*. \qquad \text{(C2)}$$

Thus in the estimation of the source energy spectral density (eqs 7 and 8), because we use the autocorrelation of the geophone recordings, we have to divide the estimation by ω^2 to estimate the displacement source energy spectral density (Fig. 5).

The division is not necessary in the waveform inversions. Because the real crosscorrelations are for velocity, we need to transfer $G_{mp}G^*_{np}$ from displacement to velocity in the forward model (eq. 11) and the source kernel (eq. 13). The transfer requires multiplying by ω^2, and thus the division cancels with the multiplication. Therefore, we do not need to divide or multiply by ω^2 in the inversions. This is only done in Fig. 5 because we wish to show the source energy spectral density for the displacement Green's function.